OPEN ACCESS



A Carbon/Oxygen-dominated Atmosphere Days after Explosion for the "Super-Chandrasekhar" Type Ia SN 2020esm

Georgios Dimitriadis^{1,2}, Ryan J. Foley¹, Nikki Arendse³, David A. Coulter¹, Wynn V. Jacobson-Galán^{4,5}, Arendse³, David A. Coulter¹, Wynn V. Jacobson-Galán^{4,5}, Arendse³, David A. Coulter¹, Wynn V. Jacobson-Galán^{4,5}, Nikki Arendse³, David A. Coulter¹, Wynn V. Jacobson-Galán^{4,5}, Wynn V. Jacobson-Galán^{4,5}, David A. Coulter¹, Wynn V. Jacobson-Galán^{4,5}, David A. Coulter¹, Wynn V. Zacobson-Galán^{4,5}, David A. Coulter¹, Wynn V. Zacobson-Galán^{4,5}, David A. Coulter¹, Wynn V. Zacobson-Galán^{4,5}, David A. Coulter^{4,5}, Wynn V. Coulter^{4,5}, Wynn V. Coulter⁴ Matthew R. Siebert 1, Luca Izzo 3, David O. Jones 1, Charles D. Kilpatrick 4, Yen-Chen Pan 6, Kirsty Taggart 1, Kirsty Taggart 1, Charles D. Kilpatrick 4, Yen-Chen Pan 6, Kirsty Taggart 1, Charles D. Kilpatrick 4, Yen-Chen Pan 6, Kirsty Taggart 1, Charles D. Kilpatrick 4, Yen-Chen Pan 6, Kirsty Taggart 1, Charles D. Kilpatrick 4, Yen-Chen Pan 6, Kirsty Taggart 1, Charles D. Kilpatrick 4, Yen-Chen Pan 6, Kirsty Taggart 1, Charles D. Kilpatrick 4, Yen-Chen Pan 6, Kirsty Taggart 1, Charles D. Kilpatrick 4, Yen-Chen Pan 6, Kirsty Taggart 1, Charles D. Kilpatrick 4, Yen-Chen Pan 6, Kirsty Taggart 1, Charles D. Kilpatrick 4, Yen-Chen Pan 6, Kirsty Taggart 1, Charles D. Kilpatrick 4, Yen-Chen Pan 6, Kirsty Taggart 1, Charles D. Kilpatrick 4, Yen-Chen Pan 6, Kirsty Taggart 1, Charles D. Kilpatrick 4, Yen-Chen Pan 6, Kirsty Taggart 1, Charles D. Kilpatrick 4, Yen-Chen Pan 6, Kirsty Taggart 1, Charles D. Kilpatrick 4, Yen-Chen Pan 6, Kirsty Taggart 1, Charles D. Kilpatrick 4, Charles D. Kilp Katie Auchettl^{1,3,7,8}, Christa Gall³, Jens Hjorth³, Daniel Kasen^{5,9}, Anthony L. Piro¹⁰, Sandra I. Raimundo^{3,11,12}, Enrico Ramirez-Ruiz¹, Armin Rest^{13,14}, Jonathan J. Swift¹⁵, and Stan E. Woosley¹ Department of Astronomy and Astrophysics, University of California, Santa Cruz, California, 95064, USA; dimitrig@tcd.ie School of Physics, Trinity College Dublin, The University of Dublin, Dublin 2, Ireland ³ DARK, Niels Bohr Institute, University of Copenhagen, Jagtvej 128, DK-2200 Copenhagen, Denmark ⁴ Center for Interdisciplinary Exploration and Research in Astrophysics (CIERA) and Department of Physics and Astronomy, Northwestern University, Evanston, IL 60208, USA ⁵ Department of Astronomy and Astrophysics, University of California, Berkeley, CA 94720, USA ⁶ Institute of Astronomy, National Central University, 300 Jhongda Road, 32001 Jhongli, Taiwan School of Physics, The University of Melbourne, VIC 3010, Australia ⁸ ARC Centre of Excellence for All Sky Astrophysics in 3 Dimensions (ASTRO 3D), Australia ⁹ Nuclear Science Division, Lawrence Berkeley National Laboratory, 1 Cyclotron Road, Berkeley, CA, 94720, USA The Observatories of the Carnegie Institution for Science, 813 Santa Barbara Street, Pasadena, CA 91101, USA

11 Department of Physics and Astronomy, University of Southampton, Highfield, Southampton SO17 1BJ, UK

12 Department of Physics and Astronomy, University of California, Los Angeles, CA 00005, USA Department of Physics and Astronomy, University of California, Los Angeles, CA 90095, USA ¹³ Department of Physics and Astronomy, Johns Hopkins University, 3400 North Charles Street, Baltimore, MD 21218, USA Space Telescope Science Institute, 3700 San Martin Drive, Baltimore, MD 21218, USA

15 The Thacher School, 5025 Thacher Road, Ojai, CA 93023, USA Received 2021 October 5; revised 2021 December 18; accepted 2021 December 20; published 2022 March 7

Abstract

Seeing pristine material from the donor star in a type Ia supernova (SN Ia) explosion can reveal the nature of the binary system. In this paper, we present photometric and spectroscopic observations of SN 2020esm, one of the best-studied SNe of the class of "super-Chandrasekhar" SNe Ia (SC SNe Ia), with data obtained -12 to +360 days relative to peak brightness, obtained from a variety of ground- and space-based telescopes. Initially misclassified as a type II supernova, SN 2020esm peaked at $M_B = -19.9$ mag, declined slowly ($\Delta m_{15}(B) = 0.92$ mag), and had particularly blue UV and optical colors at early times. Photometrically and spectroscopically, SN 2020esm evolved similarly to other SC SNe Ia, showing the usual low ejecta velocities, weak intermediate-mass elements, and the enhanced fading at late times, but its early spectra are unique. Our first few spectra (corresponding to a phase of $\gtrsim 10$ days before peak) reveal a nearly pure carbon/oxygen atmosphere during the first days after explosion. This composition can only be produced by pristine material, relatively unaffected by nuclear burning. The lack of H and He may further indicate that SN 2020esm is the outcome of the merger of two carbon/oxygen white dwarfs. Modeling its bolometric light curve, we find an 56 Ni mass of $1.23^{+0.14}_{-0.14}$ M_{\odot} and an ejecta mass of $1.75^{+0.32}_{-0.20}$ M_{\odot} , in excess of the Chandrasekhar mass. Finally, we discuss possible progenitor systems and explosion mechanisms of SN 2020esm and, in general, the SC SNe Ia class.

Unified Astronomy Thesaurus concepts: Supernovae (1668); White dwarf stars (1799) *Supporting material:* data behind figure, machine-readable tables

1. Introduction

Observations of type Ia supernovae (SNe Ia) first showed that the expansion of the universe is accelerating (Riess et al. 1998; Perlmutter et al. 1999). SNe Ia are also key to measuring the local expansion rate (Riess et al. 2016; Freedman et al. 2019), and those measurements differ from inferences from early universe probes that may indicate unaccounted physics in the current cosmological model (Freedman 2021). While there is strong observational evidence that SNe Ia result from the thermonuclear explosion of a degenerate carbon/oxygen white dwarf (WD) star in a binary system (Bloom et al. 2012), details

Original content from this work may be used under the terms of the Creative Commons Attribution 4.0 licence. Any further distribution of this work must maintain attribution to the author(s) and the title of the work, journal citation and DOI.

of the progenitor system and explosion are poorly constrained (Maoz et al. 2014).

The peak luminosity of most SNe Ia correlates strongly with their decline rate (or light-curve width, parameterized with their magnitude decline from peak to 15 days after, Δm_{15} ; Phillips 1993) and color (Riess et al. 1996). By observing the brightness, decline rate, and color of an SN Ia, one can infer its relative distance, which in turn, can be used to constrain cosmological parameters (e.g., Scolnic et al. 2018; Jones et al. 2019). The width–luminosity relation (WLR) can be explained as all SNe Ia having a similar ejecta mass with varying amounts of radioactive ⁵⁶Ni (Kasen & Woosley 2007), which sets the peak luminosity. Alternatively, the total ejecta mass may be the primary factor that causes differences in ⁵⁶Ni and luminosity (Goldstein & Kasen 2018). Moreover, SNe Ia are characterized by maximum-light spectra that lack hydrogen and helium emission features, but have prominent absorption features from

intermediate-mass (e.g., Ca, S, Si) and iron-group elements (Filippenko 1997; Parrent et al. 2014).

A small fraction of SNe Ia are outliers in the WLR (Taubenberger 2017), perhaps because of deviations in ejecta mass or ⁵⁶Ni, and not identifying such events in a distance-independent way could bias cosmological results (Rubin et al. 2015).

One of the most intriguing peculiar subclasses of SNe Ia is the "super-Chandrasekhar" SNe Ia (SC SNe Ia). The moniker for this subclass comes from modeling that suggests a total mass that is in excess of the Chandrasekhar mass (M_{Ch}; Chandrasekhar 1931), the theoretical maximum mass for a non-rotating, zero-temperature WD. Many (but not all) SC SNe Ia do not conform to the WLR, generally having peak luminosities higher than expected for their decline rate. SC SNe Ia have slowly declining light curves, high early-time UV flux, an i-band primary maximum several days before the B-band maximum, a lack of a secondary maximum in the i and near-IR (NIR) bands, relatively hot photospheres, abnormally low ejecta velocities, a weak (or delayed) NIR H-band break, and relatively strong carbon features in peak-light spectra (Ashall et al. 2021). Modeling their light curves in the same way as typical SNe Ia (Arnett 1982; Jeffery 1999), one finds that their total ejecta mass, and occasionally the 56Ni mass alone, is in excess of the Chandrasekhar mass, $M_{\rm Ch} \approx 1.4~M_{\odot}$ (Scalzo et al. 2010).

Prime examples of SC SNe Ia include SNe 2003fg (Howell et al. 2006), 2006gz (Hicken et al. 2007; Maeda et al. 2009), 2007if (Scalzo et al. 2010; Yuan et al. 2010), 2009dc (Yamanaka et al. 2009; Silverman et al. 2011; Taubenberger et al. 2011; Hachinger et al. 2012), 2012dn (Chakradhari et al. 2014; Parrent et al. 2016; Yamanaka et al. 2016; Taubenberger et al. 2019), LSQ14fmg (Hsiao et al. 2020), ASASSN-15pz (Chen et al. 2019), and ASASSN-15hy (Lu et al. 2021). Of these events, the best-studied ones are SNe 2009dc and 2012dn, coincidentally representing the significant diversity within SC SNe Ia: While SN 2009dc shows all of the observational characteristics mentioned above, SN 2012dn is noticeably fainter at peak (matching the luminosity of normal SNe Ia) with higher ejecta velocities compared to its subclass.

Late-time observations of SC SNe Ia are invaluable tools in order to shed light on the peculiar nature of these objects. Taubenberger et al. (2013) performed the first systematic study of SC SNe Ia at late epochs, finding low ionization states based on the weak [Fe III] emission lines due to high central densities, and a sudden rapid fading of their light curves (with SN 2007if being the exception, at least at the epoch of its observation), interpreted as flux redistribution into infrared wavelengths, with the source of this effect (CO formation, dust formation, γ -ray and/or positron escape, IR catastrophe, discontinued circumstellar interaction) still being debated. Moreover, Yamanaka et al. (2016) presented a late-time NIR excess of SN 2012dn, coinciding with its optical fading, while its nebular spectra show a prominent emission feature at \sim 6300 Å, which Taubenberger et al. (2019) identified as [O I] $\lambda\lambda$ 6300, 6364.

From a theoretical perspective, a definitive explosion mechanism and progenitor scenario for SC SNe Ia still do not exist. The earliest suggestion of a rapidly differentially rotating massive WD (Yoon & Langer 2005) is challenged by more recent numerical simulations (Pfannes et al. 2010a, 2010b; Fink et al. 2018). A merger of two WDs (Iben & Tutukov 1984; Webbink 1984) that exceed M_{Ch} can naturally explain the high ejecta mass (Moll et al. 2014), while increased luminosity at

early times can be achieved with hydrogen-free circumstellar medium (CSM) of material ejected during the merger in the close vicinity of the system (Raskin & Kasen 2013; Raskin et al. 2014; Noebauer et al. 2016); however, an open question remains whether this binary configuration can lead to a type Ia explosion or an accretion-induced collapse (see Marsh et al. 2004; Saio & Nomoto 2004; Dan et al. 2011; Shen et al. 2012, for relevant discussions). On the other hand, Hsiao et al. (2020), Ashall et al. (2021), and Lu et al. (2021) favor an explosion of a C–O degenerate core inside a carbon-rich envelope (Hoeflich & Khokhlov 1996), possibly under the "core-degenerate" scenario (Kashi & Soker 2011).

In this paper, we present observations of the SC SN Ia 2020esm, with excellent photometric and spectroscopic coverage, from \sim 12 days before to \sim 360 days after maximum light. We show that SN 2020esm has a nearly pure carbon/oxygen atmosphere for the first days after explosion, an observation in accordance with the merger of two carbon/oxygen WDs, providing the strongest evidence yet that WD mergers produce SNe Ia. We additionally detect early blue UV/optical colors, indicating interaction between the SN and a significant fraction of the disrupted WD that was ejected into the circumstellar environment. Finally, we confirm previous late-time observations of SC SNe Ia that show an enhanced fading at the optical light curves. We present the discovery of SN 2020esm, discuss its initial misclassification and summarize our observing campaign in Section 2. The host-galaxy properties, its distance and extinction on the line of sight, alongside its photometric and spectroscopic evolution are presented in Section 3. We discuss our findings in the context of the general SC SNe Ia population and their proposed progenitor systems in Section 4. Finally, we conclude in Section 5.

Throughout this paper, we will use the moniker SC SNe Ia to describe the members of the "super-Chandrasekhar" SNe Ia class. We note that, in the literature, different monikers have been proposed, such as 09dc-like in Taubenberger et al. (2019) and 03fg-like in Ashall et al. (2021); however, we choose to use the historical designation. Moreover, we adopt the AB magnitude system, unless where noted, and a Hubble constant of $H_0 = 73 \, \mathrm{km \, s^{-1} \, Mpc^{-1}}$.

2. Observations and Data Reduction

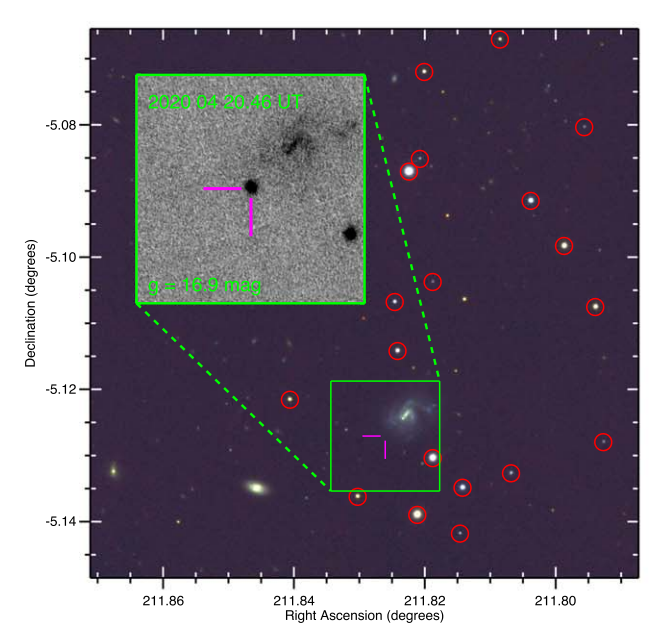
In this Section, we present the discovery of SN 2020esm, its initial classification, and our subsequent photometric and spectroscopic follow-up campaign.

2.1. Discovery and Classification

SN 2020esm was discovered on UT 2020 March 22.37 by All-Sky Automated Survey for Supernovae (ASAS-SN; Shappee et al. 2014), with an internal name of ASASSN-20dl (Brimacombe et al. 2020; Stanek 2020), at $g=17.7\pm0.04$ mag, with the last non-detection from ASAS-SN on UT 2020 March 18.90, to a limiting magnitude of 18.5. ¹⁶ The last non-detection of the transient with ZTF was on UT 2020 March 6.48 to a limiting magnitude of 19.67 in the g band, while the last non-detection with ATLAS was on UT 2020 March 16.66 to a limiting magnitude of 17.73 in the o band.

The supernova is located at $\alpha = 14^{\text{h}}07^{\text{m}}18^{\text{s}}.260$, $\delta = -05^{\circ}07'37''.67$ (J2000.0), 10."9 East, and 11."8 South of

¹⁶ https://asas-sn.osu.edu/



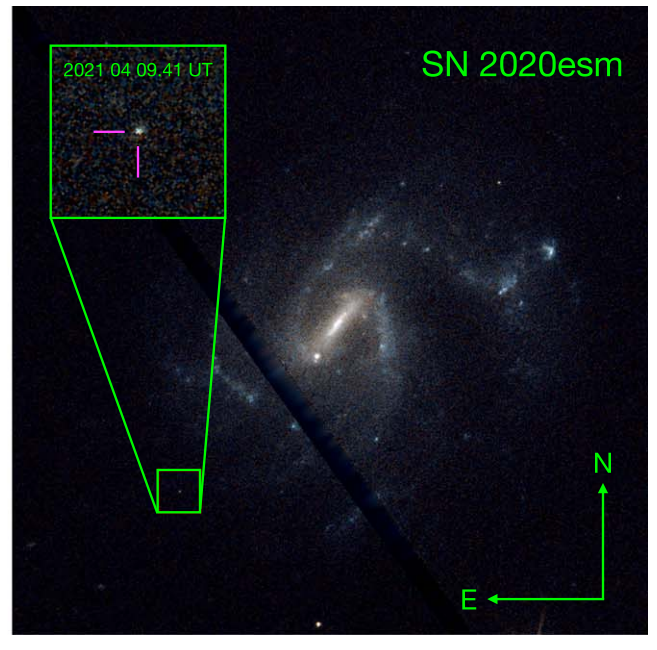


Figure 1. Pan-STARRS $5' \times 5'$ color composite (g/i/y, left) and HST/WFC3 $45'' \times 45''$ color composite (F555W/F814W, right) image stamp of the field of WISEA J140717.48-050726.1, the host of SN 2020esm. The location of the SN is indicated with the magenta tick-marks. PS1 standard stars in the field are marked with red circles. The green insets show zoomed-in regions, centered on the SN location $(1' \times 1', \text{left})$ and $3'' \times 3'', \text{right})$, taken at a phase of 14.35 and 356.02 rest-frame days from the *B*-band maximum.

WISEA J140717.48-050726.1, a star-forming irregular galaxy at a redshift of $z = 0.03619 \pm 0.00015$ (Jones et al. 2009). In Figure 1, left panel, we present a deep pre-explosion color composite (g/i/y) image stamp of WISEA J140717.48-050726.1, with the location of SN 2020esm marked with magenta tick-marks, while the green inset shows a zoomed-in region of a g-band Pan-STARRS image stamp of the supernova, at a phase of 14.35 rest-frame days from B-band maximum.

Originally, SN 2020esm was classified as a young Type II supernova (Tucker et al. 2020), based on a spectrum taken on UT 2020 March 23.45 (~1.08 days after discovery) with the University of Hawaii 2.2 m telescope (UH88) Supernova Integral Field Spectrograph (Lantz et al. 2004). That classification was the result of misclassifying the C II absorption at \sim 6300 Å and \sim 7000 Å as a P-Cygni H α feature. Moreover, based on its distance and minimal extinction on the line of sight (Section 3.1), SN 2020esm was discovered at an absolute magnitude of -18.4 ± 0.15 , indicating a luminous event, generally not consistent with core-collapse SNe. Examination of spectra taken at later phases (Figure 3) clearly shows that SN 2020esm is an SN Ia, and particularly of the SC subclass. The discovery of a candidate of one of the most rare subtypes of SNe Ia led us to initiate an extensive multiwavelength observational campaign.

2.2. Photometry

We obtained optical photometric observations of SN 2020esm with various telescopes/instruments. Our main photometry was performed with the SINISTRO cameras of the Las Cumbres Observatory Global Telescope Network (LCOGT; Brown et al. 2013) network of 1 m telescopes (NOAO2020A-012 and NOAO2020B-011, PI: Foley). Images were obtained in *ugri*, from 2020 March 25 UT (approximately 3 days after discovery and 11 days before peak brightness) until

2020 July 22 UT (107 days after maximum). Additional *griz* photometry was obtained through the Young Supernova Experiment (YSE; Jones et al. 2021) with the Pan-STARRS1 telescope (PS1) between 2020 March 25 UT and 2020 July 24 UT, *BVgri* photometry with the 1 m telescope at the Lulin observatory in Taiwan, and *griz* photometry with the 0.7 m telescope of the Thacher observatory in California (J. J. Swift et al. 2022, in preparation). Late-time *griz* imaging (at 280 and 305 days from maximum brightness) was performed with the Gemini Multi-Object Spectrograph (GMOS) on the 8.1 m Gemini North telescope in Maunakea (GN-2020B-Q-324 and GN-2021A-DD-102, PI: Foley) and *F*555*W* and *F*814*W* imaging with HST/WFC3 at 356 days from maximum brightness (SNAP-16239, PI: Foley).

All ground-based images were reduced, resampled, and calibrated using PHOTPIPE (Rest et al. 2014) with absolute flux calibration performed using PS1 standard stars in the SN field. For the HST/WFC3 photometry, reduced images were downloaded from the Mikulski Archive for Space Telescopes and drizzled following the techniques of Kilpatrick & Foley (2018). Aperture photometry was performed with photutils (Bradley et al. 2020) using a 0.12 aperture, and instrumental magnitudes were calibrated using AB zero-point conversions in the fits headers. No difference imaging was performed, as the background light from the host galaxy is minimal.

UV photometric observations were performed with the Ultraviolet Optical Telescope (UVOT; Roming et al. 2005) on board the Neil Gehrels Swift Observatory (Gehrels et al. 2004) from 2020 March 24 UT until 2020 March 30 UT, with template images obtained on 2020 March 21 UT. Aperture photometry on the difference images was performed in a 5" region on the SN location, following the standard guidelines from Brown et al. (2009), using the most recent calibration database (CALDB, version 20201008).

We present the complete SN 2020esm light curves, corrected for MW extinction, in Figure 2, spanning from -11.89 to

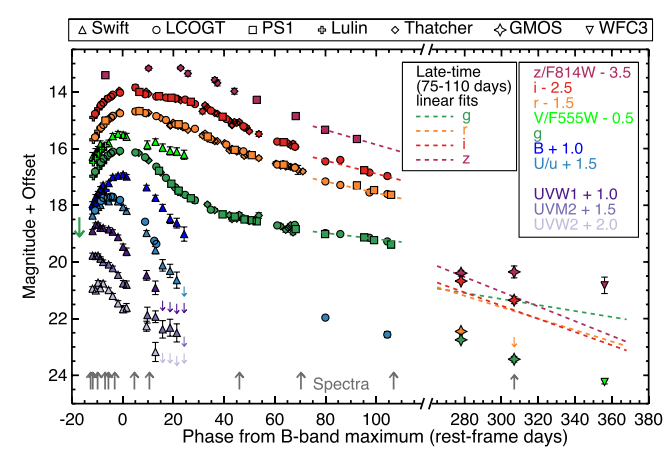


Figure 2. Multicolor light curves (UV + uBgVriz + WFC3) of SN 2020esm in rest-frame days, with respect to B-band maximum. The light curves are plotted with offsets, as described in the legend. Downward arrows mark non-detections at the location of the SN. The dashed lines shown in the late-time regime are linear fits to the 75–110 days griz light curves, extended at the phase of our late-time observations. We additionally show, with upward arrows, the phases corresponding to our spectral series (Table A2).

+356.02 days relative to peak *B* brightness, which we estimate by fitting a polynomial to the *B*-band Swift light curve from MJD 58935.0 to 58958.0, to be at MJD $_{\rm max}^B=58944.585$. Our complete photometric data set is reported in Table A1. We note that no attempt for cross-filter corrections and K-corrections was made.

2.3. Spectroscopy

Spectroscopic coverage of SN 2020esm ranges from roughly -12 to +307 days relative to the *B*-band maximum. We obtained a total of seven spectroscopic observations with the Folded Low Order whYte-pupil Double-dispersed Spectrograph (FLOYDS) spectrograph on the Faulkes 2 m telescopes of the LCOGTN; Brown et al. 2013) robotic network (NOAO2020A-012, PI: Foley), one spectrum with the Kast spectrograph (Miller & Stone 1993) on the Lick Shane telescope (2020A-S011, PI: Foley), two spectra with the Low-Resolution Imaging Spectrometer (LRIS; Oke et al. 1995) on the Keck I telescope (2020A-U209, PI: Foley), and one spectrum with GMOS (Hook et al. 2004) on the Gemini North telescope (GN-2021A-DD-102, PI: Foley).

The spectra were reduced using standard IRAF/PYRAF¹⁷ and python routines for bias/overscan subtractions and flat-fielding. The wavelength solution was derived using arc lamps while the final flux calibration and telluric lines removal were performed using spectrophotometric standard star spectra, obtained the same night (Silverman et al. 2012).

Figure 3 shows the -13 days to +107 days from *B*-band peak brightness spectral series (the spectrum at +307 days is presented and analyzed at Section 3.3). Detailed information of each observation is provided in Table A2 and the complete spectroscopic data set is available in the electronic edition.

3. Analysis

In this Section, we discuss the host galaxy of SN 2020esm, its distance and extinction along the line of sight, and we

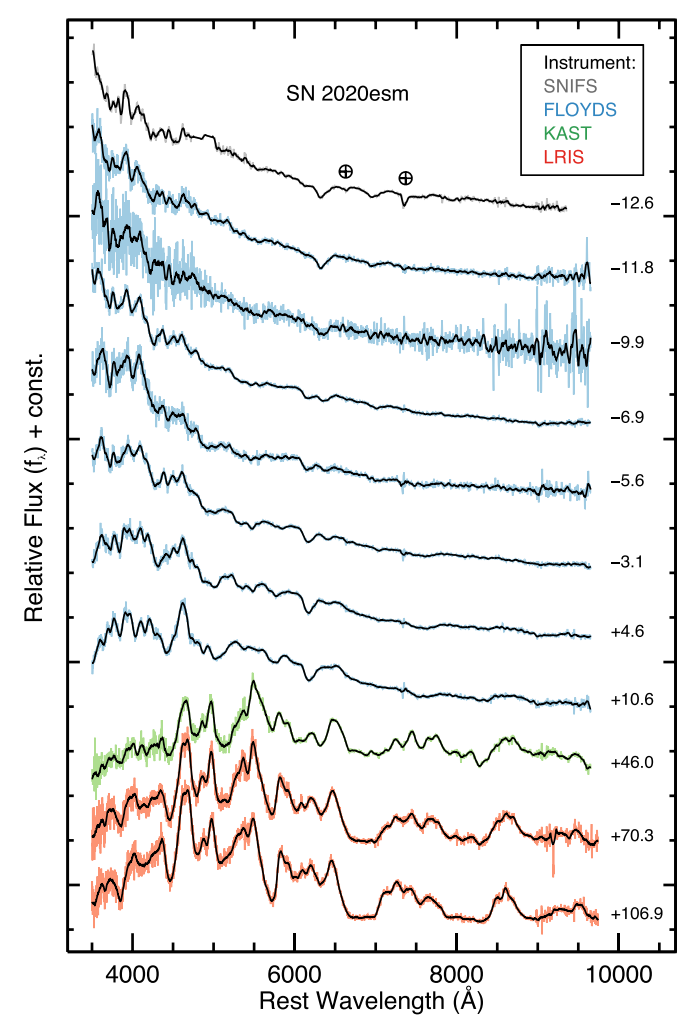


Figure 3. The spectroscopic series of SN 2020esm, spanning from -13 days to +107 days from B-band peak brightness. Each spectrum is color-coded according to each source, indicated in the legend. The black lines correspond to the smoothed versions of the spectra, using a Savitsky-Golay filter, with each spectrum's phase additionally labeled. The spectra have been corrected for Milky Way extinction $(E(B-V)_{\rm MW}=0.0207)$ and placed in rest-frame wavelength (z=0.03619).

(The data used to create this figure are available.)

present our analysis of its photometric and spectroscopic data set. Throughout our analysis, we will use data for SN 2009dc from Taubenberger et al. (2011), Brown et al. (2014), Silverman et al. (2011), and Friedman et al. (2015), for SN 2012dn from Taubenberger et al. (2019), Brown et al. (2014), and Yamanaka et al. (2016), and for SN 2011fe from Pereira et al. (2013), Zhang et al. (2016), Brown et al. (2012), and Matheson et al. (2012). We note that, while all of these SNe were photometrically observed primarily in the *UBVRI* bands, they all have excellent spectrophotometric coverage, and using these spectra, we can estimate *ugri* light curves, and directly compare them with the light curves of SN 2020esm.

3.1. Host Galaxy, Distance, and Extinction

The host galaxy of SN 2020esm is the star-forming irregular galaxy WISEA J140717.48-050726.1, at a redshift of $z\!=\!0.03619\pm0.00015$ (Jones et al. 2009). An estimate of the distance based on fitting the SN light curves (a usual method

¹⁷ IRAF is distributed by the National Optical Astronomy Observatory, which is operated by the Association of Universities for Research in Astronomy under a cooperative agreement with the National Science Foundation.

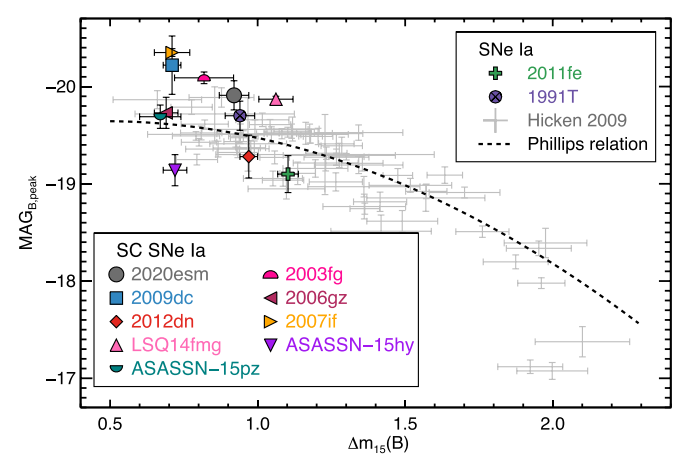


Figure 4. The absolute *B*-band magnitude vs. $\Delta m_{15}(B)$ of SNe Ia. Gray crosses correspond to the CfA SNe Ia sample from Hicken et al. (2009), with the dashed line showing the Phillips relation. We overplot SN 2020esm with a gray circle, and various other SC SNe Ia as described in the legend. The normal SN 2011fe is shown with a green cross and the overluminous SN 1991T is shown with a purple circle with X.

for determining distances) is not possible, since SN 2020esm is not a normal SN Ia, as it is brighter for its light-curve shape. With no redshift-independent distances available, we choose to use the cosmological distance of $D=156.8\pm11.0\,\mathrm{Mpc}$ ($H_0=73.0\pm5.0\,\mathrm{km\,s^{-1}\,Mpc^{-1}}$ and correcting for peculiar motions related to the Virgo cluster and Great Attractor; Mould et al. 2000). At this distance, SN 2020esm is located 12.2 kpc from the galaxy's core.

The Milky Way extinction on the line of sight is $E(B-V)_{\rm MW}=0.0207\pm0.0007$ mag, using the Schlafly & Finkbeiner (2011) dust maps. Regarding host-galaxy extinction, the large (projected) distance of the SN to its host galaxy indicates minimal extinction. Visual inspection of our high-resolution Keck/LRIS spectra shows no obvious narrow Na I D absorption at the host redshift. Using these spectra, we are able to provide a 3σ upper limit of the Na I D absorption lines equivalent width of $EW_{\rm upper}=0.072$ Å, and assuming a Fitzpatrick (1999) reddening law with $R_V=3.1$, this corresponds to an upper limit of $E(B-V)_{\rm host}=0.017\pm0.012$ mag (Poznanski et al. 2012, with updated uncertainty as per Phillips et al. 2013). Thus, we use only the Milky Way reddening on the line of sight, and we adopt this value to correct all of our photometry and spectra.

SC SNe Ia tend to explode in relatively low-mass galaxies, with high specific star formation rate (sSFR), with events hosted by more massive galaxies tending to explode in remote locations (Taubenberger et al. 2011). In order to place SN 2020esm in the context of SC SN Ia host galaxies, we derive a stellar mass and star formation rate (SFR) for WISEA J140717.48-050726.1 using the SED fitting package LE PHARE (Arnouts et al. 1999; Ilbert et al. 2006). The code uses the population-synthesis templates of Bruzual & Charlot (2003), summed according to an exponentially declining burst of star formation. We assume a Chabrier (2003) initial mass function and a stellar metallicity set between 0.2-1.0 Z_{\odot} . Dust attenuation in the galaxy is applied to the SED models using the Calzetti et al. (2000) template. As an input, we performed elliptical aperture photometry on PS1 (Chambers et al. 2016) images in grizy bands, using PS1 field stars for calibration, and corrected all photometry for foreground extinction. We find a stellar mass of $\log(M/M_{\odot}) = 9.72^{+0.05}_{-0.03}$ and an SFR of

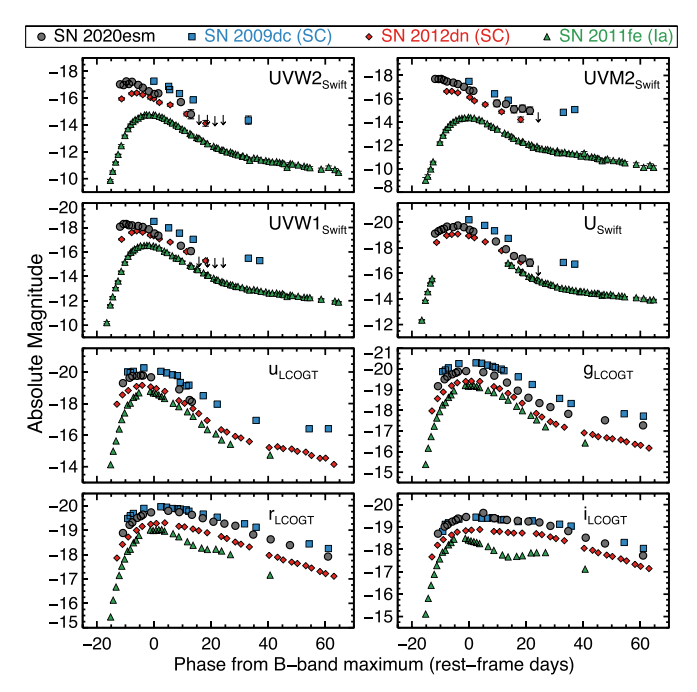


Figure 5. The UV (Swift *UVW2*, *UVM2*, *UVW1*, and *U*) and optical (*ugri*) light curves of SN 2020esm (gray circles) are presented in absolute magnitude. The light curves are compared with the light curves of SN 2009dc (blue squares), SN 2012dn (red diamonds), and SN 2011fe (green upward triangles).

 $\log(M/M_{\odot}~{\rm yr^{-1}}) = -0.07^{+0.51}_{-0.67}~~(\log {\rm sSFR}~({\rm yr^{-1}}) = -9.79).$ For consistency, we performed the same analysis for the host galaxies of SNe 2009dc and 2012dn, finding stellar masses of $\log(M/M_{\odot}) = 10.67^{+0.04}_{-0.06}~~{\rm and}~~\log(M/M_{\odot}) = 9.65^{+0.05}_{-0.08},~{\rm with}~~{\rm SFRs}~\log(M/M_{\odot}~{\rm yr^{-1}}) = -0.50^{+0.52}_{-0.89}~~{\rm and}~~\log(M/M_{\odot}~{\rm yr^{-1}}) = 0.11^{+0.32}_{-0.06}~({\rm log~sSFR}~({\rm yr^{-1}}) = -11.17~~{\rm and}~-9.54),~{\rm respectively}.$

3.2. Photometric Evolution

SN 2020esm peaked in the *B* band on 2020 April 5 UT, at $B=16.16\pm0.03$ mag and taking into account the distance to WISEA J140717.48-050726.1 and the extinction on the line of sight (Section 3.1), the peak absolute *B*-band magnitude was -19.91 ± 0.15 mag. The magnitude decline in the *B* band after 15 days was $\Delta m_{15}(B)=0.92\pm0.05$ mag, comparable to other high-luminosity/slowly declining SC SNe Ia ($\Delta m_{15}(B)=0.97$ and 0.71 mag for SN 2012dn and SN 2009dc, respectively, as opposed to $\Delta m_{15}(B)=1.1$ mag for the normal SN 2011fe; Figure 4).

We show the absolute magnitude light curves of SN 2020esm in Figure 5. SN 2020esm displays several characteristics associated with SC SNe Ia in contrast to normal SNe Ia: it is substantially brighter at peak (\sim 2–3 mag brighter in the UV and \sim 1 mag in the optical), shows a slower evolution of the light curve in all wavelengths, and lacks the distinctive secondary maximum in the redder bands. Of particular interest are the UV light curves: while SN 2011fe showed a steep rise from around -15 days and peaked at -1.7 (UVW2), -0.2 (UVM2), and -2.3 (UVWI) days from the B-band maximum, SN 2020esm is close to peak or fading from our first observations (-12 days from the B-band maximum). The general evolution of the light curves matches the SC SNe Ia, closely resembling SN 2009dc, although somewhat fainter, while being brighter than SN 2012dn.

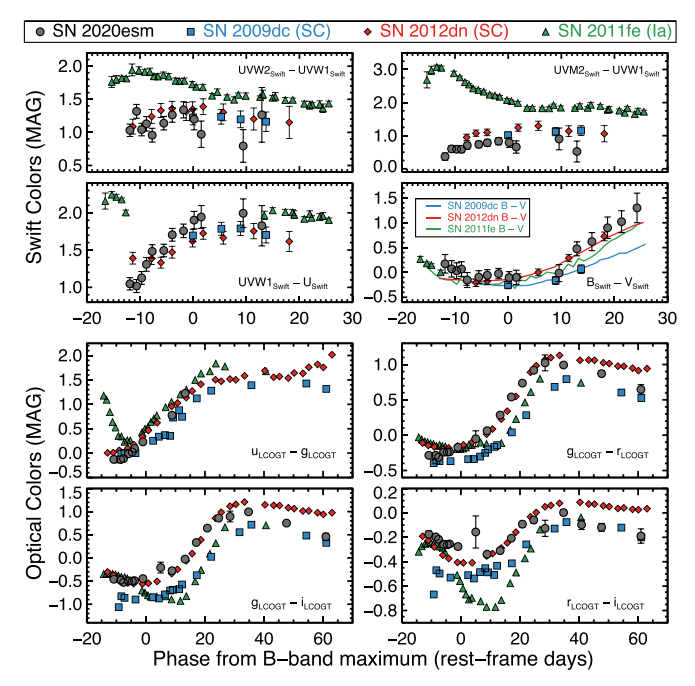


Figure 6. The Swift (UVW2-UVW1, UVM2-UVW1, UVW1-U, and B-V) and optical (u-g, g-r, g-i, and r-i) color curves of SN 2020esm (gray circles), compared with SN 2009dc (blue squares), SN 2012dn (red diamonds), and SN 2011fe (green upward triangles). For the Swift B-V panel, we additionally plot ground-based B-V color curves for each SN, as solid lines.

Figure 6 shows the Swift and optical color evolution of SN 2020esm. The observed early colors are considerably bluer than those of normal SNe Ia, particularly in the UV, due to the small amount of line blanketing and the weak Ca II H&K absorption feature (Figure 3). Another characteristic of SC SNe Ia, is the optical color evolution in r-i from peak up to about +30 days, when normal SNe Ia show their bluest colors, while SC SNe Ia continuously evolve to redder colors, a behavior seen in SN 2020esm.

The evolution of the light curve changes dramatically at later times (Figure 2). Our *griz* observations at \sim 280 and \sim 305 days from *B*-band maximum show that the *g*- and *r*-band luminosities are substantially fainter than expected from linear fits at the 75–110 day regime (\sim 1.7–2.0 and \sim 1.3 mag, respectively), while the *i* and *z* bands have faded less (only \sim 0.35 and \sim 0.1–0.9 mag, respectively), with the *z* band showing a (nearly) constant evolution. Similar evolution is seen in the HST photometry (at \sim 356 days, Figure 1, right), where the *F*555*W* (*V* -band equivalent) is substantially faint, while *F*814*W* (wide *I*) remains bright.

This photometric behavior is remarkably similar to SN 2009dc (Taubenberger et al. 2011): its R-band light curve continues its earlier phase linear decline, while the B band at \sim 260 days from maximum is \sim 0.7 mag fainter, and the I band at \sim 295 days from maximum is \sim 0.9 mag brighter, relative to their linear declines, with an analogous behavior (although observed with fewer data) seen in the SC SN 2006gz (Maeda et al. 2009). A more drastic change is observed in LSQ14fmg and SN 2012dn even earlier: the optical light curves start to rapidly fade after \sim 30 and 60 days from maximum, respectively, with a simultaneous increase of the NIR luminosity, which has been attributed to either pre-existing dust in an NIR echo scenario (Yamanaka et al. 2016) or the CO formation/dust formation in the SN ejecta (Taubenberger et al.

2019; Hsiao et al. 2020). We note that, while we have not acquired NIR photometry for SN 2020esm at these epochs, there is no indication of a dramatic shift of the emission to longer wavelengths, as our z-band observations, although brighter than expected, do not show an increase in brightness, ruling out the formation of a significant amount of dust.

This change in decline rates (seen also in the bolometric light curves; Section 3.4) is in contrast with normal SNe Ia (such as SN 2011fe; Zhang et al. 2016) that have consistent late-time declines until ~ 500 days (Dimitriadis et al. 2017). Moreover, the rapid fading is inconsistent with the canonical SN Ia radioactive decay evolution, where the (bolometric) decline rate is expected to slow down after $\sim 250-300$ days from maximum, and resemble the 56 Co decay rate. This shared characteristic of SC SNe Ia indicates a common explosion mechanism for this subclass of thermonuclear explosions, potentially different from normal SNe Ia. We defer to Section 4 for further discussion on the physical mechanisms that may lead to this unexpected behavior.

3.3. Spectroscopic Evolution

Figure 7 shows early (left), peak (top right), and late (bottom right) spectra of SN 2020esm, compared to the SC SNe Ia 2009dc and 2012dn, the normal SNe Ia 2011fe, the SLSN 2017egm, and the SN II 2017eaw.

The early spectra of SN 2020esm (Figures 3 and 7, left) are unique among known thermonuclear WD SNe. The spectra are dominated by a blue continuum with a strong absorption feature at \sim 6300 Å and a somewhat weaker one at \sim 7000 Å. We model the -11.8-day spectrum with SYN++ (Thomas et al. 2011), a parameterized SN spectral synthesis software. SYN++ treats the SN as an optically thick, continuum-emitting pseudophotosphere surrounded by a line-forming region of various atomic elements, and assumes spherical symmetry, local thermal equilibrium, and homologous expansion of the ejecta. While this generalized approach might not accurately describe the physical conditions in the SN, it is useful for inferring the presence (or absence) of specific atomic species at various ejecta velocities and ionization states. Our main results are shown in Figure 8, where the gray and blue lines correspond to SNe 2020esm and 2009dc, respectively, at similar phases. Our full fit for SN 2020esm is shown as a black solid line.

The continuum is well described with a blackbody of T = 15,500 K, on which we add C II at $\sim 12,800 \text{ km s} - 1$ (red line), detached from the photosphere (\sim 11,500 km s⁻¹), in order to reproduce the flat emission peak and the sharp red edge of the \sim 6300 Å P-Cygni absorption feature. There is an indication of a weak absorption feature at ~6000 Å, which could be Si II at the photospheric velocity. However, as can be seen by comparing SN 2020esm with SN 2009dc, other intermediate-mass elements (IMEs), such as S II and Ca II, are absent or extremely weak. This suggests that silicon is either absent or extremely weak at these early phases (substantially weaker that SN 2009dc). On the contrary, the absorption features at 3500-4800 Å are adequately matched with O II (orange line). While other IMEs might be present, although extremely weak, the spectrum can be generally reproduced with only C II and O II, giving additional evidence of a nearly pure carbon/oxygen atmosphere above the expanding photosphere. This spectrum is similar to the earliest spectra of some superluminous SNe (thought to have core-collapse progenitors; Quimby et al. 2018), but later spectra of SN 2020esm are

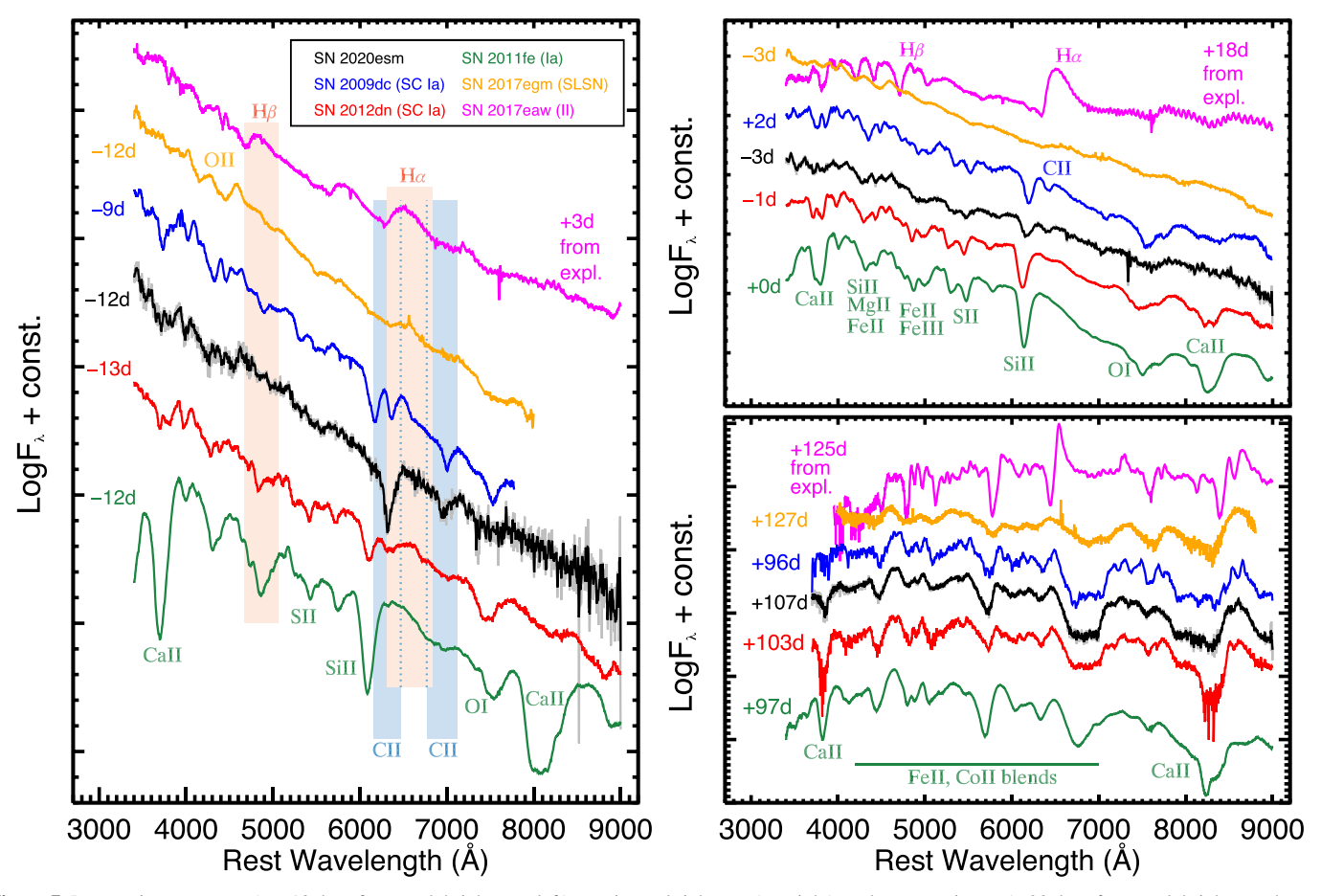


Figure 7. Pre-maximum spectra (< -10 days from peak brightness, left), maximum brightness (top right), and post-maximum (>90 days from peak brightness, bottom right) of SN 2020esm, compared to the normal type Ia SN 2011fe, two SC SNe Ia (SN 2009dc and SN 2012dn), the SLSN SN 2017egm (Nicholl et al. 2017), and the Type II SN 2017eaw (Szalai et al. 2019). All spectra are in flux density per unit wavelength, F_{λ} , and presented in logarithmic scale with additional offsets, for presentation purposes. Orange-shaded regions represent the H α and H β at \pm 12,000 km s⁻¹ (typical ejecta velocities of early hydrogen-rich core-collapse SNe), while the blue-shaded ones correspond to C II at -20,000 to -5000 km s⁻¹ (typical ejecta velocities of unburnt material, seen in early thermonuclear SNe). Other intermediate-mass and iron-peak elements, present in normal SNe Ia spectra, are marked with green labels, while the O II line blend, identified in SL SNe, is marked in orange. The phases relative to each SN's maximum are additionally labeled.

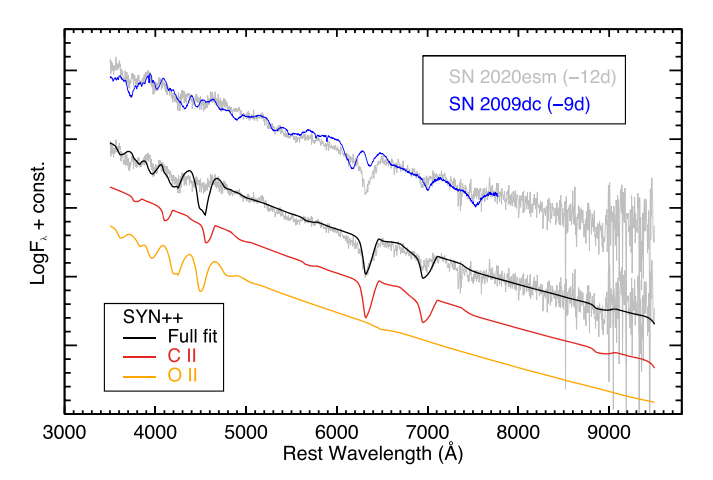


Figure 8. The early spectrum of SN 2020esm is shown as a gray line. Our best fit is shown as a black line, which consists of a 15,500 K blackbody, with C II and O II, with the decomposition of the atomic species shown as red and orange lines, respectively. We additionally show the early (\sim -9 day) spectrum of SN 2009dc as a blue line.

distinct from those of that class. With only a single early spectrum, one might incorrectly classify an SN similar to SN 2020esm as an SN II (as was done for SN 2020esm) or an

SLSN, potentially contaminating samples of those classes (see Jerkstrand et al. 2020 for a similar case of a potential misclassification of SN 2006gy).

As the SN evolves toward peak brightness, the usual IMEs seen in thermonuclear SNe (e.g., O I, Mg II, Ca II, Si II, S II, Fe II, and Fe III) start to appear, although considerably weaker, in accordance with SC SNe Ia (Figure 7, top right). At this phase, the SN has evolved to a clear thermonuclear one, confirming the misclassification of it as a core collapse. The ejecta velocities and strengths of the unburned and synthesized products, probed by C II and Si II, respectively, are estimated by fitting these two features with Gaussian profiles across our spectral series, with our results shown in Figure 9.

The ejecta velocities, probed by the IME Si II, remain approximately constant throughout SN 2020esm's evolution, with a velocity similar to SN 2009dc (and substantially lower than SN 2011fe). However, the C II velocity is higher than both SN 2009dc and SN 2012dn, up to \sim -5 days, indicating that unburnt material at early times is located above the photosphere. Moreover, the equivalent width of the C II line is particularly high, and becomes similar in strength to that of SN 2009dc around maximum light, after which the C II and Si II velocities become comparable, suggesting that the unburnt material is mixed with IMEs in lower layers of the ejecta.

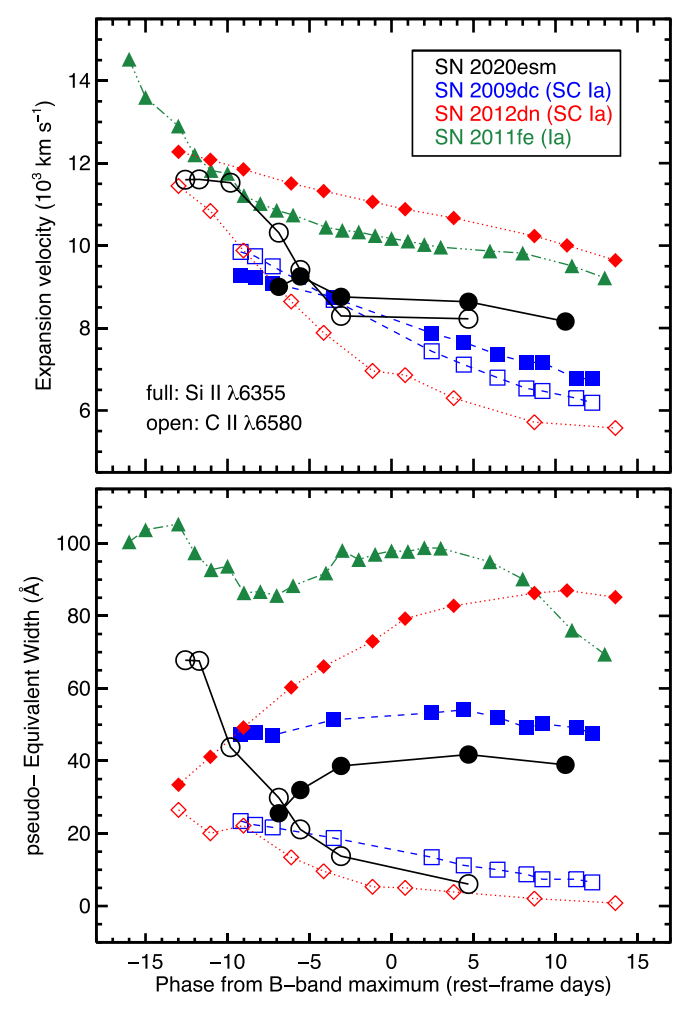


Figure 9. The expansion velocity (top) and pseudo- equivalent width (bottom) of Si II $\lambda 6355$ (full symbols) and C II $\lambda 6580$ (open symbols) as a function of phase for SN 2020esm (black circles), SN 2009dc (blue squares), SN 2012dn (red diamonds), and SN 2011fe (green upward triangles). Typical uncertainties are $\sim 200 \, \mathrm{km \ s^{-1}}$ and $\sim 5 \, \mathring{\mathrm{A}}$, respectively.

Figure 10, left panel, shows our +307 days spectrum of SN 2020esm (black), compared with nebular spectra of SN 2009dc (blue), SN 2012dn (red), and SN 2011fe (green) at similar phases. While the signal-to-noise ratio of the spectrum, particularly at bluer wavelengths, is not high, common nebular SC SNe Ia features, such as [Fe III], [Fe II], and [Ni II], can be seen. A defining characteristic of SC SNe Ia is the relatively low [Fe III] flux relative to [Fe II] as probed by the $\lambda4700/\lambda5200$ line ratio. The lower ratio of these lines in SC SNe Ia is attributed to a lower ionization state at these epochs and higher central ejecta densities, compared to normal SNe Ia (Mazzali et al. 2011; Taubenberger et al. 2013).

The line complex of SC SNe Ia at ~7000–7500 Å differs from normal SNe Ia, which are dominated by forbidden transitions of [Fe II] and [Ni II]. SN 2020esm is more similar to SN 2009dc and SN 2012dn, with two sharp emission peaks in this wavelength range. We attempt to fit the ~7000–7500 Å line complex for the nebular spectra of SNe 2020esm, 2009dc, 2012dn, and 2011fe with a similar approach as in Graham et al. (2017), Maguire et al. (2018), and Siebert et al. (2020), with the results shown in the right panel of Figure 10. While for the normal SN 2011fe, the line complex can be adequately fit with only [Fe II] and [Ni II] emission, the SC SNe Ia require an

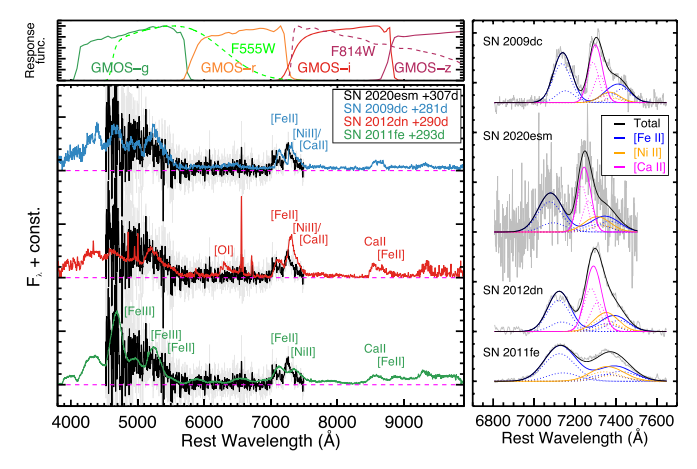


Figure 10. The late-time (\sim 307 days from peak brightness) raw (gray) and binned (black) spectrum of SN 2020esm is shown in the left panel. Late-time spectra at similar phases are shown for SN 2009dc (blue), SN 2021dn (red), and SN 2011fe (green). Various spectral features of normal and SC SNe Ia present in nebular epochs are marked with green and blue/red labels, respectively. In the upper panel, we show the response functions of the GMOS griz and HST-WFC3 F555W and F814W filters, with solid and dashed lines, respectively. On the right panel, the \sim 7000–7500 Å line region of each SN is shown, with the model fits overplotted, as in the legend.

additional [Ca II] component. This likely detection of [Ca II] is consistent with the lower ionization state of SC SNe Ia, compared to normal SNe Ia, as [Ca II] is a very efficient cooling line and dominates the emission features, if calcium exists in the same ejecta region as other Fe-group elements. Moreover, as can be seen in the upper panel, the i, z, and F814W bands probe the line complexes of $\sim 7000-7500$ and $\sim 8500-9000$ Å corresponding to regions of the spectrum where [Ca II] and the calcium NIR triplet emission are expected, respectively, while the r band is free of strong emission lines, probing the bolometric decline due to the radioactive decay of 56 Ni. The photometric evolution of this band at late phases (Section 3.2), with the substantial fading in the gr bands and the constant evolution of the iz bands, in conjunction with the +307 day spectrum, confirms this line identification.

Interestingly, SN 2020esm shows much higher (blueshifted) iron/nickel and calcium velocities (-3300 and -2400 km s⁻ compared to SN 2009dc $(-800 \text{ and } -115 \text{ km s}^{-1})$ and SN 2012dn (-1500 and $-520 \,\mathrm{km \, s^{-1}}$). This substantial net blueshift of the lines can be interpreted as the formation of dust in the ejecta, as the newly formed dust can obscure more emission from the far side of the SN, causing a suppression of the redshifted emission, and an asymmetric line profile (Smith et al. 2008). However, the line ratio of [Fe II]/[Ni II] of SN 2020esm is similar to the one of the dust-free SN 2011fe $(3.02 \pm 0.54 \text{ and } 2.91 \pm 0.02, \text{ respectively})$, indicating that this blueshift is not an effect of a line asymmetry. This spectroscopic observation, in combination with the late-time photometry (see Section 3.2), may rule out the formation of dust. Unlike SN 2012dn, we do not detect [O I] $\lambda\lambda$ 6300,6364, and we place an upper limit of the [OI] luminosity at $2.5 \times 10^{36} \,\mathrm{erg \, s^{-1}}$. Finally, we also do not detect H α , with an upper limit of the luminosity at $1.7 \times 10^{36} \, \mathrm{erg \, s^{-1}}$.

3.4. Bolometric Light Curve

We constructed a pseudo-bolometric light curve from our UV optical photometry as follows: after correcting our UV and optical photometric magnitudes for Milky Way extinction, we

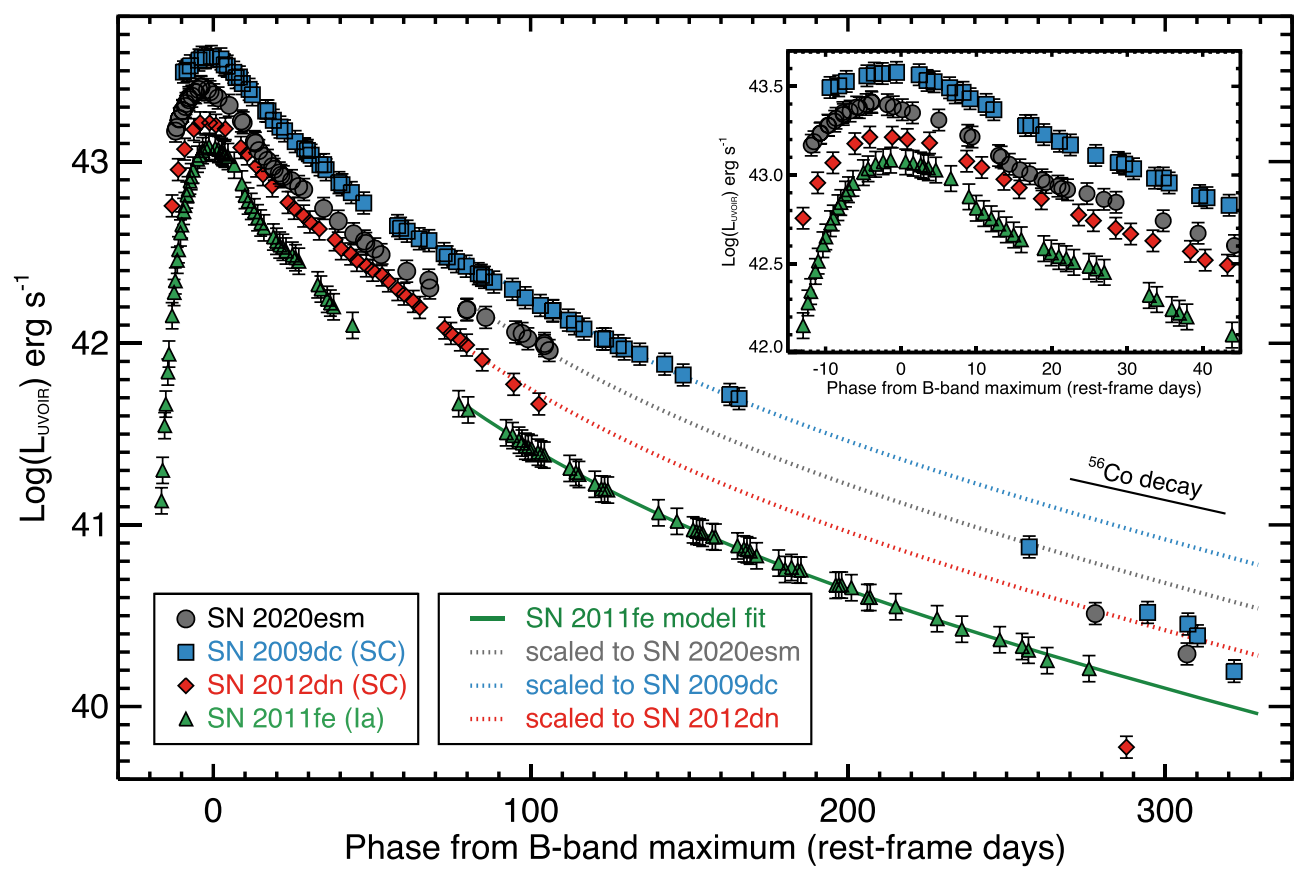


Figure 11. The constructed bolometric light curve of SN 2020esm (gray circles), compared to the bolometric light curves of the normal SN 2011fe (green upward triangles) and the SC SNe 2009dc (blue squares) and 2012dn (red diamonds), in units of erg s $^{-1}$, with the inset showing the zoomed-in region around peak luminosity. At late times, the solid green line is a fit to the bolometric light curve of SN 2011fe, as described in the text, with the dotted gray, blue, and red lines showing the fit scaled to SN 2020esm, SN 2009dc, and SN 2012dn, respectively. The slope of the 56 Co radioactive decline rate is shown as a solid black line.

converted them to monochromatic fluxes. For the case of missing observations in any of the optical bands on a given epoch, an estimation was made with linear interpolation on adjacent epochs, while for the UV light curves after 2020 April 30 UT, we assumed zero flux. The final spectral energy distribution was interpolated linearly and integrated with respect to wavelength. We assumed zero flux at the blue end of the UVW2 band (1600 Å) and at the red end of the i band (10000 Å). Finally, we used the luminosity distance to the SN to convert the integrated flux to luminosity. For the NIR wavelength regime (10000-24000 Å), we used bolometric corrections derived from SN 2009dc, which shows similar color evolution in the UV and optical bands (however, see Ashall et al. 2021 for the variations at early NIR light curves of SC SNe Ia). Adding this NIR luminosity to our UV and optical one, we derive a total pseudo-bolometric UVOIR light curve, as a function of phase from the B-band maximum, shown in Figure 11, with gray circles, and presented in Table 1. We additionally show the bolometric light curves of SN 2009dc (blue squares), SN 2012dn (red diamonds), and SN 2011fe (green upward triangles), which were constructed using a similar procedure (note that SN 2009dc, SN 2012dn, and SN 2011fe have extensive coverage in the NIR; thus, the NIR

luminosity is directly computed, contrary to SN 2020esm). In order to estimate the ⁵⁶Ni and the ejecta mass of SN 2020esm, we use the Markov chain Monte Carlo code PYBOLOSN (Scalzo et al. 2014). The code fits the late-time bolometric light curve, with the ⁵⁶Ni and the ejecta mass as free

Table 1 UVOIR Bolometric Light of SN 2020esm

Phase ^a (rest-frame days)	$\frac{L}{(10^{43} \text{ erg s}^{-1})}$	$ \begin{array}{c} L \text{ Error} \\ (10^{43} \text{ erg s}^{-1}) \end{array} $	
-11.90	1.472	0.203	
-11.54	1.541	0.213	
-10.74	1.717	0.237	
-10.65	1.726	0.238	

Note. The complete bolometric light curve is available.

(This table is available in its entirety in machine-readable form.)

parameters, and the rise time of the bolometric light curve as a prior. In this calculation, we assume that the pseudo-bolometric luminosity of the SN is only due to the radioactive decay of $^{56}\rm{Ni}$. We performed the same analysis for SN 2011fe, SN 2012dn, and SN 2009dc, using rise time priors that are reported in their relevant studies: $t_{\rm rise}^{11\rm fe}=16.6\pm0.15,$ $t_{\rm rise}^{12\rm dn}=20.0\pm0.5,$ and $t_{\rm rise}^{09\rm dc}=22.0\pm0.5$ days. Due to the uncertain time of explosion of SN 2020esm, but motivated by its similar light-curve evolution with the one of SN 2009dc, we choose $t_{\rm rise}^{20\rm esm}=22.0\pm2.0$ days. The results are shown in Figure 12, with our final estimates reported in Table 2. Our results place SN 2020esm comfortably in the SC SNe Ia regime, particularly in terms of the ejecta mass.

^a Relative to *B*-band maximum (MJD 58944.58).

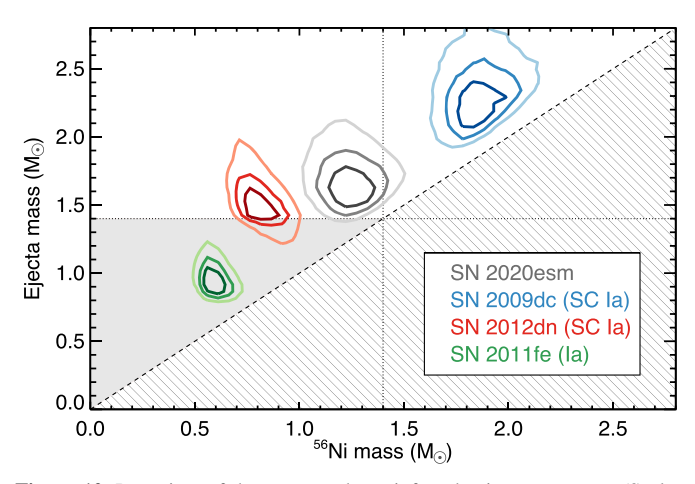


Figure 12. Posteriors of the $M_{56}_{\rm Ni}$ and $M_{\rm ej}$ inferred using PYBOLOSN (Scalzo et al. 2014). The contours for each SN correspond to the 25, 50, and 75 percentiles. Dotted horizontal and vertical lines mark the classical Chandrasekhar mass limit (1.4 M_{\odot}), with the gray-shaded region corresponding to the sub-Chandrasekhar region. The forbidden $M_{56}_{\rm Ni} > M_{\rm ej}$ region is crossed out.

As can be seen in Figure 11, the decline rate of the bolometric light curve of SN 2020esm changes dramatically at later times. SN 2020esm shows a similar decline rate as SN 2009dc, and is substantially brighter than SN 2011fe. The decline rate is significantly faster than the $^{56}\mathrm{Co}$ decay (shown with the solid black line in Figure 11), and is attributed to the increasing escape fraction of the γ -rays, as the opacity of the ejecta decreases. We do not detect the increasing fading seen in SN 2012dn after $\sim\!60$ days from peak, which indicates that none of the proposed mechanisms that led to this rapid decline in SN 2012dn's luminosity (as proposed in Taubenberger et al. 2019) have occurred yet. However, at much later phases ($\sim\!280$ days), we observe a decline in the bolometric luminosity, similar to SN 2009dc.

We fit the late-time (50–300 days) bolometric light curve of SN 2011fe with a simple 56 Co radioactive decay model that takes into account the decreasing optical depth to the γ -rays, while the positrons and X-rays entirely deposit their energy in the ejecta (i.e., we consider the positrons and X-rays fully trapped). Under these assumptions, the bolometric luminosity from the 56 Co decay chain is:

$$L = \frac{2.221 \times 10^{43}}{56} \frac{\lambda_{56}}{\text{days}^{-1}} \frac{M_{56}}{M_{\odot}} \frac{q_{56}^{\gamma} f_{56}^{\gamma}(t) + q_{56}^{l} + q_{56}^{X}}{\text{keV}}$$

$$\times \exp(-\lambda_{56}t) \text{ erg s}^{-1}$$

where M_{56} is the initial mass synthesized, λ_{56} is the decay constant, q_{56}^{γ} , q_{56}^{l} , and q_{56}^{χ} are the average energies per decay carried by γ -rays, positrons, and X-rays, and f_{56}^{γ} is the fraction of the γ -rays that contribute to the luminosity, and is given by $f_{56}^{\gamma}(t) = 1 - \exp(-(t_{56}^{\gamma}/t)^2)$, where t_{56}^{γ} corresponds to the time when the optical depth to γ -rays becomes unity. The values for the decay energies and constants were obtained from the National Nuclear Data Center. This simple toy model can reasonably well reproduce the late-time emission of normal SNe Ia, as seen for the case of SN 2011fe (green solid line) up to \sim 300 days. We find $M_{56} = 0.29 \pm 0.04 M_{\odot}$ and $t_{56}^{\gamma} = 38.9 \pm 4.7$ days, in tension with the estimate from the

Table 2
Estimates of ⁵⁶Ni and Ejecta Mass of SN 2020esm, SN 2009dc, SN 2012dn, and SN 2011fe

SN Name	M 56 $_{ m Ni}$ $({ m M}_{\odot})$	$M_{ m ej} \ ({ m M}_{\odot})$
SN 2020esm	$1.23^{+0.14}_{-0.14}$	$1.75^{+0.32}_{-0.20}$
SN 2009dc	$1.84^{+0.17}_{-0.14}$	$2.34^{+0.26}_{-0.22}$
SN 2012dn	$0.82^{+0.12}_{-0.10}$	$1.56^{+0.33}_{-0.18}$
SN 2011fe	$0.60^{+0.07}_{-0.06}$	$1.00^{+0.19}_{-0.11}$

Note. Uncertainties are reported as 1σ percentiles.

peak luminosity ($M_{56} = 0.6 M_{\odot}$), a result that has also been confirmed in other studies (Zhang et al. 2016; Dimitriadis et al. 2017; Shappee et al. 2017), with possible explanations including positron escape, additional flux beyond the UVOIR wavelength regime, or an infrared catastrophe.

We scale the SN 2011fe fit to match the 50-100 days bolometric light curves of the SC SNe Ia, shown in Figure 11 as gray, blue, and red dotted lines, for SN 2020esm, SN 2009dc, and SN 2012dn, respectively. While the model fairly matches the light curves at these epochs, the steeper decline rate at later times is obvious, notably occurring earlier for SN 2012dn. The luminosity of SN 2020esm evolves similarly to SN 2009dc, with a decrease of flux at \sim 278 and \sim 307 days, when we find that SN 2020esm has 53% and 44% of the scaled SN 2011fe model, while for SN 2009dc, at \sim 295–320 days, we find 37%– 24% and for SN 2012dn, at \sim 288 days, 20%. Assuming similar conditions in the ejecta of the SNe and applying scaling relations for the nickel masses according to SN 2011fe, we measure nickel masses from the 56 Co radioactive tail of $M_{56} = 0.29 \pm 0.06 \, M_{\odot}$ for both SN 2020esm and SN 2009dc, and $M_{56} = 0.08 \pm 0.02 \, M_{\odot}$ for SN 2012dn. We defer to Section 4 for further discussion on the physical mechanisms that may lead to this unexpected behavior.

4. Discussion

In this Section, we discuss our findings in the context of the proposed progenitor models of the SC SNe Ia class. In particular, the main observables of SN 2020esm that any viable candidate model needs to address are its early spectra, its early blue UV/optical colors, its high luminosity and slow decline rate, and its enhanced optical fading at later times.

As mentioned above (Section 1), the earliest suggestion for the origin of an SC SN Ia was the explosion of a single C/O WD, with mass >M_{Ch}, which is able to sustain this mass while rapidly rotating or in the presence of high magnetic fields (Yoon & Langer 2005). This scenario was initially proposed for the first SC SN Ia 2003fg (Howell et al. 2006). However, Fink et al. (2018), using state-of-the-art numerical simulations, showed that, while this set of models can potentially predict the high luminosity and slow decline rate of (most, but not all) SC SNe Ia (due to the high nickel and ejecta masses involved), they cannot explain their spectral characteristics, as they fail to reproduce the low ejecta velocities at peak, and the detonation that unbinds the WD does not leave any unburnt carbon in the ejecta. This is in contrast with spectral observations of SC SNe Ia, particularly with SN 2020esm (Figures 3 and 8), where strong absorption features of carbon (and potentially oxygen) are identified at early times.

https://www.nndc.bnl.gov/

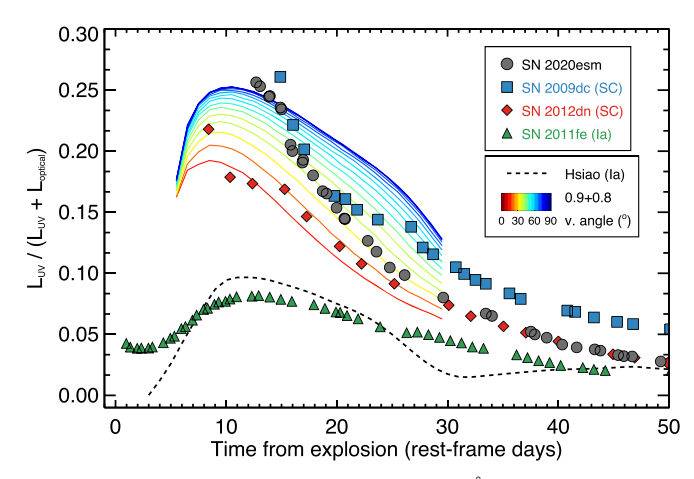


Figure 13. The ratio of the UV (1600–3000 Å) to the UV+optical (1600–10000 Å) luminosity of SN 2020esm (gray circles) compared with SN 2009dc (blue squares), SN 2012dn (red diamonds), and SN 2011fe (green upward triangles). We additionally show, with the black dashed line, the same ratio of the Hsiao et al. (2007) template, representing the normal SNe Ia, and with the red-to-blue color scheme lines, the merger model of $0.9M_{\odot} + 0.8M_{\odot}$ WDs from Raskin et al. (2014). The viewing angle dependence is illustrated in the legend.

For about a week after explosion, SN 2020esm continued to have an atmosphere consisting of principally carbon and oxygen. While some normal SNe Ia have carbon lines early in their evolution, their spectra are dominated by absorption from intermediate-mass and even iron-group elements only a few hours after explosion, consistent with the explosion of a compact WD (Nugent et al. 2011; Foley et al. 2012). However, the persistent carbon and oxygen absorption features of SN 2020esm imply a large mass of unburnt material in the outermost layers of the ejecta. The only way to have as much pristine, unburnt material as SN 2020esm is an extended envelope of material above the exploding WD. This configuration can be achieved by disrupting a C/O WD during the process of merging with another (more massive) WD (Moll et al. 2014). This process should leave a relatively large fraction of the disrupted WD just above the burnt material, which would be immediately swept up by the ejecta to produce the early C II and O II absorption (Raskin et al. 2014).

Hydrodynamical models of this merger process also expect a sizable fraction of the disrupted WD to be unbound or barely bound to the system, producing a large amount of CSM (Raskin & Kasen 2013). There may be a delay between the disruption and explosion, and the density and radius of the CSM should scale with the delay. That is, prompt explosions should have dense material close to the star, while delayed explosions could have material at large radii. Some merger systems, in particular those with unequal masses, are also expected to eject material well before they merge and potentially detonate (Dan et al. 2011, 2012).

Another natural delay is the viscous timescale for the accretion disk formed from the disrupted WD, ranging from minutes to days (Raskin & Kasen 2013). The CSM would expand at roughly the escape speed, resulting in material out to as much as 10¹⁴ cm. The SN shock would quickly interact with this material, resulting in additional UV/X-ray photons, and the shock-heated material would cool on the diffusion time, creating additional UV photons (Piro 2012).

Figure 13 shows the UV (1600–3000 Å) contribution of SN 2020esm to the bolometric light curve. SN 2020esm along

with the SC SNe Ia 2012dn and 2009dc emit substantially more in the UV regime at early times, when the UV emission constitutes almost 20%–25% of the UV+optical luminosity. compared to the normal SN 2011fe. We additionally compare with the UV contribution of the $0.9M_{\odot} + 0.8M_{\odot}$ WDs merger model from Raskin et al. (2014), a violent merger model of two WDs, where the detonation occurs after the secondary WD is disrupted, forming a disk of carbon and oxygen material around the primary WD. The outcome of the simulation is a synthesized spectral series, as a function of the time from explosion and the viewing angle, with 0° and 90° denoting viewing angles along the pole and along the equator, respectively. The viewing angle orientation has strong observational effects in the model spectra, with the UV contribution being higher along the equator, likely due to reduced line blanketing; as the ejecta collide with the disk, ⁵⁶Ni is slowed down to low velocities, resulting in the absence of iron-group elements above the photosphere and weak line blanketing.

Another strong orientation effect of the Raskin et al. (2014) models is the velocity and strength of the unburnt carbon and the IMEs absorption features. For equatorial viewing angles, the surrounding disk decelerates the ejecta, additionally narrowing their velocity range above the photosphere. This can be seen in Figure 14, where the model spectra (especially the ones along the equator, for which silicon/carbon is weaker/stronger with lower/higher velocities than the ones along the pole) qualitatively match the spectra of SN 2020esm, showing the strong carbon features (although at larger velocities) and the blue continuum. While the model does not exactly match the observations of SN 2020esm, it shows distinct observables, such as the weak IMEs, the blue color, and the persistent carbon, that normal SNe Ia (represented by the Hsiao et al. 2007 template) do not show.

While the merger models from Raskin et al. (2014) are able to reproduce the general spectroscopic properties of SN 2020esm, they generally cannot fully reproduce the (bolometric) light curves of SC SNe Ia. Figure 15 shows the constructed bolometric light curves of the $0.9M_{\odot} + 0.8M_{\odot}$ and $1.2M_{\odot}+1.0M_{\odot}$ models, compared to SN 2020esm. This models produce 0.664(1.23) M_{\odot} of $^{56}{\rm Ni}$ with a total ejecta mass of 1.77(2.20) M_{\odot} , respectively. SN 2020esm is $1.5-2.7 \times$ brighter at peak, compared to the model at 90° (along the equator) and 0° (along the pole), respectively. Higher-mass models are able to roughly match the peak luminosity (as they produce more ⁵⁶Ni), but they predict slower decline rates, as the total ejecta mass increases. However, the Raskin et al. (2014) merger models do not include any interaction of the SN ejecta with a carbon/oxygen-rich CSM, which can naturally increase the luminosity of a low-mass merger to the luminosity of SN 2020esm. Possible origins of the CSM include material from the disrupted secondary WD (Raskin & Kasen 2013) or the (ejected) envelope of an AGB star (Kashi & Soker 2011; Hsiao et al. 2020).

An additional problem with the mergers as paths toward SC SNe Ia explosions (and in fact for all SNe Ia) is the asymmetric explosions that these models predict (Bulla et al. 2016). The two SC SNe Ia that have polarimetric observations, SN 2007if (Cikota et al. 2019) and SN 2009dc (Tanaka et al. 2010), show low levels of polarization, excluding large asymmetries. However, these observations were performed after peak brightness (13, 20, 45, and 46 days and 6 and 90 days after

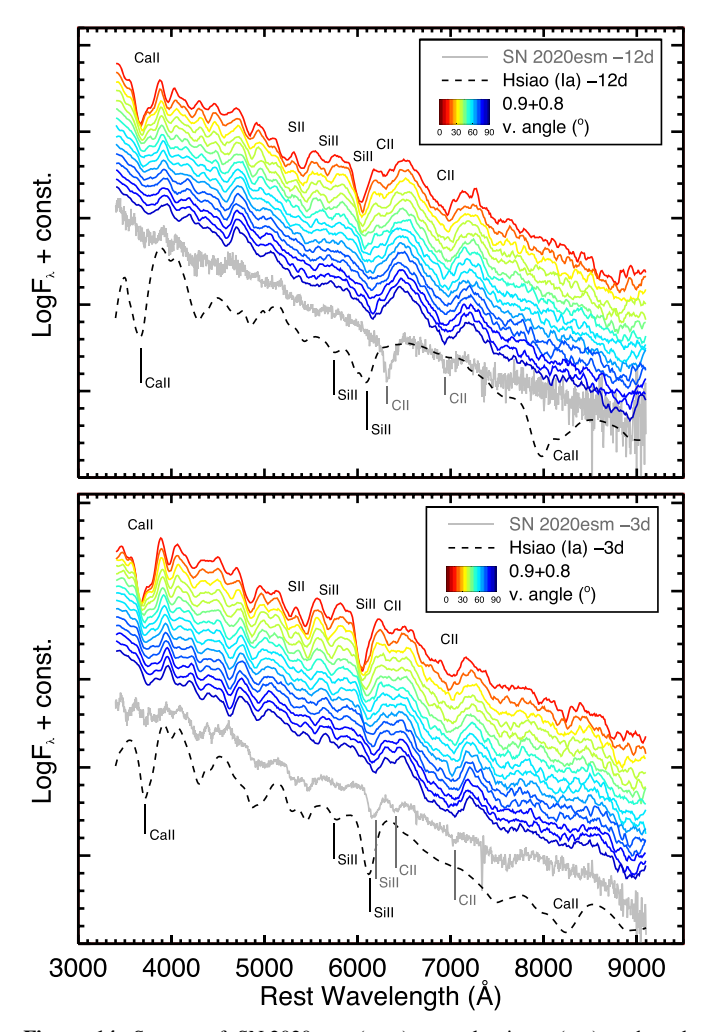


Figure 14. Spectra of SN 2020esm (gray) at early times (top) and peak brightness (bottom), compared with the Hsiao et al. (2007) template and the merger model of $0.9M_{\odot} + 0.8M_{\odot}$ WDs from Raskin et al. (2014), at similar epochs. The viewing angle dependence is illustrated in the legend. Several spectra features, discussed in the text, are additionally labeled.

maximum for SN 2007if and SN 2009dc, respectively), when the ejecta may have settled into a more spherical geometry. Nevertheless, early-time polarimetry of SC SNe Ia is crucial to provide insight to their explosion mechanism.

We note that there is a significant debate about the exact conditions that lead to a detonation during a double C/O WD binary merger and the time delay between the initiation of the merger and the subsequent explosion. In particular, it has been shown (Dan et al. 2011, 2012) that during detonations at contact, the final merger may take tens to hundreds of orbits (with initial periods of hundreds of seconds), during which mass ejection from the system can take place, creating a carbon/oxygen atmosphere and reproducing the observations of SN 2020esm. These models favor unequal-mass systems with high total mass, which are expected to take longer for the dynamical instability to set in and lead to the detonation, while the actual location of the hotspot can alter the synthesized ⁵⁶Ni mass. In any case, both the delayed merger models from Raskin et al. (2014) and the unequal-mass mergers with a detonation triggered close to contact can match the observables of SN 2020esm, such as the high ⁵⁶Ni and ejecta mass, the early carbon/oxygen-dominated spectra, and the blue early colors.

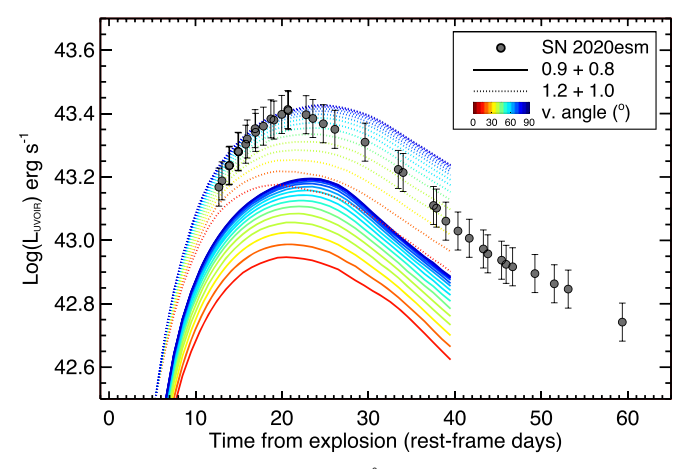


Figure 15. The bolometric (1600–24000 Å) light curve of SN 2020esm (gray circles) is compared with the $0.9M_{\odot}+0.8M_{\odot}$ (solid lines) and $1.2M_{\odot}+1.0M_{\odot}$ (dotted lines) WD merger models from Raskin et al. (2014). The viewing angle dependence is illustrated in the legend.

Finally, another striking observational characteristic of SN 2020esm is the rapid fading of the optical light curves and the enhanced decline rate of the bolometric light curve at late times (Figure 11), seen in most of SC SNe Ia. This unique behavior of SC SNe Ia has been investigated in previous studies (Silverman et al. 2011; Taubenberger et al. 2011; Taubenberger 2017; Taubenberger et al. 2019) with no definite conclusions. Initially, it was proposed that this enhanced decline rate was, in fact, a manifestation of the end of the interaction of the ejecta with CSM, a mechanism that could explain the increased peak brightness, since this interaction will result in additional luminosity, which would compensate for the normal ⁵⁶Ni-powered light curve at early times, and place SC SNe Ia at the normal SNe Ia context. However, no indication of hydrogen-rich CSM is evident, due to the absence of narrow hydrogen emission features at early times. On the other hand, hydrogen-free CSM (such as unburnt C/O material, originating from the disrupted secondary WD) is a possible explanation; however, a sustained ejecta-CSM interaction up to \sim 100–200 days after maximum is not supported by simulations. On a different approach, the enhanced decline rate could be due to a real flux deficit, with possible explanations including a change in the energy deposition rate (such as reduced γ -ray and/or positron trapping), a redistribution of the emission into longer wavelengths (such as the onset of an early IR catastrophe), or the formation of dust, which results in absorption of the optical light and re-emission of a thermal continuum, determined by the temperature of the dust. In the case of SN 2020esm, no observations in the mid-to-far-IR have been made; thus, no conclusive statements regarding the progenitor can be made.

A possible solution to the SC SNe Ia progenitor problem may be that of thermonuclear explosions inside a dense non-degenerate carbon-rich envelope (Hoeflich & Khokhlov 1996; Noebauer et al. 2016), a model suggested in Hsiao et al. (2020) and Ashall et al. (2021). This approach can generally explain most of the observables, such as the bright luminosity and slow evolution (as the interaction between the ejecta and the envelope produces a strong reverse shock that converts kinetic to luminous energy) and the low ejecta velocities (as the reverse shock decelerates the ejecta). However, these early models do not explicitly specify the origin of the envelope,

while they generally predict very large 56Ni and envelope masses to explain the slow rise. The authors invoke the "coredegenerate" scenario (Kashi & Soker 2011), the explosion of the degenerate C/O core in the center of an AGB star, as a possible progenitor scenario. Additional arguments in favor of this scenario include (i) the detection of a superwind in observations of LSQ14fmg (Hsiao et al. 2020) and (ii) the observational correlations presented in Ashall et al. (2021; a more massive envelope would produce brighter explosions, stronger carbon lines, and lower Si velocities). However, these models predict significant X-ray luminosity (due to the interaction) and a UV late-time re-brightening (due to interaction with previous superwind episodes of the AGB star), which have not been seen yet. More importantly, the interaction of the ejecta with the AGB's envelope/wind should produce narrow hydrogen/helium emission lines, an observation that has never been seen in SC SNe Ia. While this absence may be explained if the AGB star is at the late stage of its evolution, as proposed for LSQ14fmg by Hsiao et al. (2020), where the dense and non-degenerate envelope does not allow γ -rays to escape and form narrow emission features, it requires that all SC SNe Ia originate from late-stage AGB stars. At the same time, core-degenerate explosions at earlier stages of the AGB star should be common, but never seen (with a possible exception of the equally rare subclass of SNe Ia-CSM; Silverman et al. 2013). Nevertheless, this scenario is intriguing, and an exploration of its theoretical and observed rates and complete physical parameters, alongside accurate hydrodynamical, nucleosynthetic, and radiative transfer calculations, is encouraged.

5. Conclusion

In this work, we presented extensive UV and optical groundand space-based observations of the "super-Chandrasekhar" SNe Ia candidate 2020esm, spanning from a few days after explosion to its nebular epochs. SN 2020esm shares all of the basic characteristics of the SC SNe Ia subclass, such as the high luminosity at peak, the slow evolution of its light curve, the absence of the secondary maximum at the redder photometric bands, the blue early UV and optical colors, the persistent carbon features up to \sim 10 days from maximum, the low ejecta velocities, the weak IMEs absorption lines, the low ionization in the nebular spectra, and the rapid decline of the optical light curves at late times. Its early spectrum, revealing a nearly pure carbon/oxygen atmosphere, provides strong evidence of a WD merger as the progenitor system (ruling out all single WD models). Finally, we discussed theoretical models that have been proposed as viable candidates for these explosions.

We note that SN 2020esm was initially misclassified as a core-collapse event, leaving open the possibility of more SC SNe Ia incorrectly classified in the past as SNe II or SLSN based only on one spectrum, resulting in contamination of samples of these classes.

As more SC SNe Ia are discovered, the intrinsic diversity within this subclass is becoming more prevalent. Thus, the need for high-quality observations, such as early- and late-time UV observations, X-ray observations immediately after discovery, and high-resolution spectroscopy (especially at the ${\rm H}\alpha$ and helium wavelength regions) in the optical and NIR, of these events is extremely important, in order to reveal the true nature of these enigmatic events.

We thank the anonymous referee for helpful comments that improved the clarity and presentation of this paper.

The UCSC transient team is supported in part by NSF grant AST-1518052, NASA/Swift grant 80NSSC19K1386, the Gordon & Betty Moore Foundation, the Heising-Simons Foundation, and by a fellowship from the David and Lucile Packard Foundation to R.J.F.

A major upgrade of the Kast spectrograph on the Shane 3 m telescope at Lick Observatory was made possible through generous gifts from the Heising-Simons Foundation as well as William and Marina Kast. Research at Lick Observatory is partially supported by a generous gift from Google.

Some of the data presented herein were obtained at the W. M. Keck Observatory, which is operated as a scientific partnership among the California Institute of Technology, the University of California, and the National Aeronautics and Space Administration. The Observatory was made possible by the generous financial support of the W. M. Keck Foundation. The authors wish to recognize and acknowledge the very significant cultural role and reverence that the summit of Maunakea has always had within the indigenous Hawaiian community. We are most fortunate to have had the opportunity to conduct observations from this mountain.

We acknowledge the use of public data from the Neil Gehrels Swift Observatory data archive. The work made use of Swift/UVOT data reduced by P. J. Brown and released in the Swift Optical/Ultraviolet Supernova Archive (SOUSA). SOUSA is supported by NASA's Astrophysics Data Analysis Program through grant NNX13AF35G.

The Young Supernova Experiment and its research infrastructure is supported by the European Research Council under the European Union's Horizon 2020 research and innovation program (ERC grant agreement No. 101002652, PI K. Mandel), the Heising-Simons Foundation (2018-0913, PI R. Foley; 2018-0911, PI R. Margutti), NASA (NNG17PX03C, PI R. Foley), NSF (AST-1720756, AST-1815935, PI R. Foley; AST-1909796, AST-1944985, PI R. Margutti), the David & Lucille Packard Foundation (PI R. Foley), VILLUM FONDEN (project number 16599, PI J. Hjorth), and the Center for AstroPhysical Surveys (CAPS) at the National Center for Supercomputing Applications (NCSA) and the University of Illinois Urbana-Champaign.

The Pan-STARRS1 Surveys (PS1) and the PS1 public science archive have been made possible through contributions by the Institute for Astronomy, the University of Hawaii, the Pan-STARRS Project Office, the Max Planck Society and its participating institutes, the Max Planck Institute for Astronomy, Heidelberg and the Max Planck Institute for Extraterrestrial Physics, Garching, The Johns Hopkins University, Durham University, the University of Edinburgh, the Queen's University Belfast, the Harvard-Smithsonian Center for Astrophysics, the Las Cumbres Observatory Global Telescope Network Incorporated, the National Central University of Taiwan, the Space Telescope Science Institute, the National Aeronautics and Space Administration under grant No. NNX08AR22G issued through the Planetary Science Division of the NASA Science Mission Directorate, the National Science Foundation grant No. AST-1238877, the University of Maryland, Eotvos Lorand University (ELTE), the Los Alamos National Laboratory, and the Gordon and Betty Moore Foundation.

Based on observations obtained at the international Gemini Observatory (NOIRLab Prop. ID 2020B-0358 and GN-2021A-DD-102), a program of NSF's NOIRLab, which is managed by the Association of Universities for Research in Astronomy (AURA) under a cooperative agreement with the National Science Foundation on behalf of the Gemini Observatory partnership: the National Science Foundation (United States), National Research Council (Canada), Agencia Nacional de Investigación y Desarrollo (Chile), Ministerio de Ciencia, Tecnología e Innovación (Argentina), Ministério da Ciência, Tecnología, Inovações e Comunicações (Brazil), and Korea Astronomy and Space Science Institute (Republic of Korea). We thank the director, J. Lotz, and J. Blakeslee for their approval of and assistance with our DD program.

This work makes use of observations from the Las Cumbres Observatory global telescope network (NOIRLab Prop. IDs 2020A-0334 and 2020B-0250; PI: R. Foley).

This research is based on observations made with the NASA/ESA Hubble Space Telescope obtained from the Space Telescope Science Institute, which is operated by the Association of Universities for Research in Astronomy, Inc., under NASA contract NAS 5-26555. These observations are associated with program SNAP-16239.

This publication has made use of data collected at Lulin Observatory, partly supported by MoST grant 108-2112-M-008-001.

D.A.C. acknowledges support from the National Science Foundation Graduate Research Fellowship under grant DGE1339067.

W.J.-G. is supported by the National Science Foundation Graduate Research Fellowship Program under grant No. DGE-1842165 and the IDEAS Fellowship Program at Northwestern University. W.J.-G. acknowledges support through NASA grants in support of Hubble Space Telescope program GO-16075.

M.R.S. is supported by the National Science Foundation Graduate Research Fellowship Program under grant No. 1842400.

This work was supported by a VILLUM FONDEN Investigator grant to J.H. (project No. 16599) and by a VILLUM FONDEN Young Investigator grant to C.G. (project No. 25501).

Support for D.O.J. was provided by NASA through the NASA Hubble Fellowship grant HF2-51462.001 awarded by the Space Telescope Science Institute, which is operated by the Association of Universities for Research in Astronomy, Inc., for NASA, under contract NAS5-26555.

Parts of this research were supported by the Australian Research Council Centre of Excellence for All Sky Astrophysics in 3 Dimensions (ASTRO 3D), through project No. CE170100013.

Facilities: LCOGT (Sinistro and FLOYDS), PS1, Lulin, Gemini (GMOS), Swift (UVOT), HST (WFC3), Shane (Kast), Keck (LRIS).

Software: photpipe (Rest et al. 2014), iraf/pyraf (Tody 1986, 1993; Science Software Branch at STScI 2012), Le PHARE (Arnouts et al. 1999; Ilbert et al. 2006), SYN++ (Thomas et al. 2011), pyBoloSN (Scalzo et al. 2014).

Appendix

In this section we present data Tables A1 and A2 for all photometric and spectroscopic observations of SN 2020esm.

Table A1Observed Photometry of SN 2020esm

MJD	Phase ^a (rest-frame days)	Filter	Brightness (AB mag)	Brightness Error (AB mag)	Flux $(10^{-16} \text{ erg cm}^{-2} \text{ s}^{-1} \mathring{A}^{-1})$	Flux Error ($10^{-16} \text{ erg cm}^{-2} \text{ s}^{-1} \mathring{A}^{-1}$)
58932.26	-11.89	B _{Swift}	17.056	0.098	8.7400	0.7889
58932.26	-11.89	$UVW2_{Swift}$	19.126	0.070	6.0200	0.3881
58932.26	-11.89	U_{Swift}	16.967	0.055	14.9400	0.7566
58932.27	-11.88	UVW1 _{Swift}	18.053	0.062	10.3300	0.5897
58932.29	-11.86	V_{Swift}	16.860	0.159	6.6890	0.9796
58932.29	-11.86	$UVM2_{Swift}$	18.471	0.090	8.9510	0.7420
58932.63	-11.53	g_{Lulin}	17.051	0.010	7.2030	0.0663
58932.63	-11.53	$\mathrm{B}_{\mathrm{Lulin}}$	17.212	0.011	7.4280	0.0752
58932.63	-11.53	V_{Lulin}	17.049	0.009	5.4960	0.0456
58932.64	-11.53	i_{Lulin}	17.438	0.010	1.9470	0.0179
58932.64	-11.53	r_{Lulin}	17.243	0.009	3.5580	0.0295
58933.32	-10.87	i_{LCOGT}	17.314	0.022	2.2840	0.0463
58933.32	-10.87	u_{LCOGT}	16.786	0.024	16.9700	0.3752
58933.32	-10.87	g_{LCOGT}	16.891	0.013	8.5270	0.1021
58933.32	-10.87	r_{LCOGT}	17.152	0.015	3.8740	0.0535

Note. The complete photometric table is available.

(This table is available in its entirety in machine-readable form.)

^a Relative to *B*-band maximum (MJD 58944.58).

Table A2Observing Details of the Optical Spectra of SN 2020esm

Obs Date (UT)	Phase ^a (rest-frame days)	Telescope + Instrument	Slit Width	Grism/Grating	Exposure Time (s)
2020-03-24	-11.8	Faulkes North + FLOYDS	1."6	235 1/mm	2100
2020-03-26	-9.9	Faulkes North + FLOYDS	1."6	235 1/mm	1800
2020-03-29	-6.9	Faulkes North + FLOYDS	1."6	235 1/mm	1500
2020-03-30	-5.6	Faulkes South + FLOYDS	1."6	235 1/mm	1500
2020-04-02	-3.1	Faulkes North + FLOYDS	1."6	235 1/mm	1500
2020-04-10	4.6	Faulkes North + FLOYDS	1."6	235 1/mm	1500
2020-04-16	10.6	Faulkes North + FLOYDS	1."6	235 1/mm	1500
2020-05-23	46.0	Shane + Kast	2."0	452/3306 + 300/7500	1845 (blue), 3×600 (red)
2020-06-17	70.3	Keck + LRIS	1."0	600/4000 + 400/8500	610 (blue), 600 (red)
2020-07-25	106.9	Keck + LRIS	1."0	600/4000 + 400/8500	1800 (blue), 2×650 (red)
2021-02-17	306.9	Gemini North + GMOS	1."0	B600	8×900

Note. The complete spectroscopic data are available as data behind Figure 3.

ORCID iDs

Georgios Dimitriadis https://orcid.org/0000-0001-9494-179X

Ryan J. Foley https://orcid.org/0000-0002-2445-5275
Nikki Arendse https://orcid.org/0000-0001-5409-6480
David A. Coulter https://orcid.org/0000-0003-4263-2228
Wynn V. Jacobson-Galán https://orcid.org/0000-0003-1103-3409

Matthew R. Siebert https://orcid.org/0000-0003-2445-3891 Luca Izzo https://orcid.org/0000-0001-9695-8472 David O. Jones https://orcid.org/0000-0002-6230-0151 Charles D. Kilpatrick https://orcid.org/0000-0002-5740-7747

Yen-Chen Pan https://orcid.org/0000-0001-8415-6720 Kirsty Taggart https://orcid.org/0000-0002-5748-4558 Katie Auchettl https://orcid.org/0000-0002-4449-9152 Christa Gall https://orcid.org/0000-0002-8526-3963 Jens Hjorth https://orcid.org/0000-0002-4571-2306 Anthony L. Piro https://orcid.org/0000-0001-6806-0673 Sandra I. Raimundo https://orcid.org/0000-0002-6248-398X

Enrico Ramirez-Ruiz https://orcid.org/0000-0003-2558-3102

Armin Rest https://orcid.org/0000-0002-4410-5387 Jonathan J. Swift https://orcid.org/0000-0002-9486-818X Stan E. Woosley https://orcid.org/0000-0002-3352-7437

References

Arnett, W. D. 1982, ApJ, 253, 785
Arnouts, S., Cristiani, S., Moscardini, L., et al. 1999, MNRAS, 310, 540
Ashall, C., Lu, J., Hsiao, E. Y., et al. 2021, ApJ, 922, 205
Bloom, J. S., Kasen, D., Shen, K. J., et al. 2012, ApJL, 744, L17
Bradley, L., Sipőcz, B., Robitaille, T., et al. 2020, astropy/photutils: 1.0.0, 1.0.0, Zenodo, doi:10.5281/zenodo.4044744
Brimacombe, J., Krannich, G., Cacella, P., et al. 2020, ATel, 13666, 1
Brown, P. J., Breeveld, A. A., Holland, S., Kuin, P., & Pritchard, T. 2014, Ap&SS, 354, 89
Brown, P. J., Dawson, K. S., de Pasquale, M., et al. 2012, ApJ, 753, 22

Brown, P. J., Dawson, K. S., de Pasquale, M., et al. 2012, ApJ, 753, 22 Brown, P. J., Holland, S. T., Immler, S., et al. 2009, AJ, 137, 4517 Brown, T. M., Baliber, N., Bianco, F. B., et al. 2013, PASP, 125, 1031 Bruzual, G., & Charlot, S. 2003, MNRAS, 344, 1000 Bulla, M., Sim, S. A., Pakmor, R., et al. 2016, MNRAS, 455, 1060 Calzetti, D., Armus, L., Bohlin, R. C., et al. 2000, ApJ, 533, 682 Chabrier, G. 2003, PASP, 115, 763

Chakradhari, N. K., Sahu, D. K., Srivastav, S., & Anupama, G. C. 2014, MNRAS, 443, 1663 Chambers, K. C., Magnier, E. A., Metcalfe, N., et al. 2016, arXiv:1612.05560 Chandrasekhar, S. 1931, ApJ, 74, 81 Chen, P., Dong, S., Katz, B., et al. 2019, ApJ, 880, 35 Cikota, A., Patat, F., Wang, L., et al. 2019, MNRAS, 490, 578 Dan, M., Rosswog, S., Guillochon, J., & Ramirez-Ruiz, E. 2011, ApJ, 737, 89 Dan, M., Rosswog, S., Guillochon, J., & Ramirez-Ruiz, E. 2012, MNRAS, Dimitriadis, G., Sullivan, M., Kerzendorf, W., et al. 2017, MNRAS, 468, 3798 Filippenko, A. V. 1997, ARA&A, 35, 309 Fink, M., Kromer, M., Hillebrandt, W., et al. 2018, A&A, 618, A124 Fitzpatrick, E. L. 1999, PASP, 111, 63 Foley, R. J., Challis, P. J., Filippenko, A. V., et al. 2012, ApJ, 744, 38 Freedman, W. L. 2021, ApJ, 919, 16 Freedman, W. L., Madore, B. F., Hatt, D., et al. 2019, ApJ, 882, 34 Friedman, A. S., Wood-Vasey, W. M., Marion, G. H., et al. 2015, ApJS, 220, 9 Gehrels, N., Chincarini, G., Giommi, P., et al. 2004, ApJ, 611, 1005 Goldstein, D. A., & Kasen, D. 2018, ApJL, 852, L33 Graham, M. L., Kumar, S., Hosseinzadeh, G., et al. 2017, MNRAS, 472, 3437 Hachinger, S., Mazzali, P. A., Taubenberger, S., et al. 2012, MNRAS, 427, 2057 Hicken, M., Challis, P., Jha, S., et al. 2009, ApJ, 700, 331 Hicken, M., Garnavich, P. M., Prieto, J. L., et al. 2007, ApJL, 669, L17 Hoeflich, P., & Khokhlov, A. 1996, ApJ, 457, 500 Hook, I. M., Jørgensen, I., Allington-Smith, J. R., et al. 2004, PASP, 116, 425 Howell, D. A., Sullivan, M., Nugent, P. E., et al. 2006, Natur, 443, 308 Hsiao, E. Y., Conley, A., Howell, D. A., et al. 2007, ApJ, 663, 1187 Hsiao, E. Y., Hoeflich, P., Ashall, C., et al. 2020, ApJ, 900, 140 Iben, I. J., & Tutukov, A. V. 1984, ApJS, 54, 335 Ilbert, O., Arnouts, S., McCracken, H. J., et al. 2006, A&A, 457, 841 Jeffery, D. J. 1999, arXiv:astro-ph/9907015 Jerkstrand, A., Maeda, K., & Kawabata, K. S. 2020, Sci, 367, 415 Jones, D. H., Read, M. A., Saunders, W., et al. 2009, MNRAS, 399, 683 Jones, D. O., Foley, R. J., Narayan, G., et al. 2021, ApJ, 908, 143 Jones, D. O., Scolnic, D. M., Foley, R. J., et al. 2019, ApJ, 881, 19 Kasen, D., & Woosley, S. E. 2007, ApJ, 656, 661 Kashi, A., & Soker, N. 2011, MNRAS, 417, 1466 Kilpatrick, C. D., & Foley, R. J. 2018, MNRAS, 481, 2536 Lantz, B., Aldering, G., Antilogus, P., et al. 2004, Proc. SPIE, 627, 146 Lu, J., Ashall, C., Hsiao, E. Y., et al. 2021, ApJ, 920, 107 Maeda, K., Kawabata, K., Li, W., et al. 2009, ApJ, 690, 1745 Maguire, K., Sim, S. A., Shingles, L., et al. 2018, MNRAS, 477, 3567 Maoz, D., Mannucci, F., & Nelemans, G. 2014, ARA&A, 52, 107 Marsh, T. R., Nelemans, G., & Steeghs, D. 2004, MNRAS, 350, 113 Matheson, T., Joyce, R. R., Allen, L. E., et al. 2012, ApJ, 754, 19 Mazzali, P. A., Maurer, I., Stritzinger, M., et al. 2011, MNRAS, 416, 881 Miller, J. S., & Stone, R. P. S. 1993, LOTRM, https://mthamilton.ucolick. org/techdocs/instruments/kast/Tech%20Report%2066%20KAST% 20Miller%20Stone.pdf Moll, R., Raskin, C., Kasen, D., & Woosley, S. E. 2014, ApJ, 785, 105 Mould, J. R., Huchra, J. P., Freedman, W. L., et al. 2000, ApJ, 529, 786

Nicholl, M., Berger, E., Margutti, R., et al. 2017, ApJL, 845, L8

^a Relative to *B*-band maximum (MJD 58944.58).

```
Noebauer, U. M., Taubenberger, S., Blinnikov, S., Sorokina, E., &
  Hillebrandt, W. 2016, MNRAS, 463, 2972
Nugent, P. E., Sullivan, M., Cenko, S. B., et al. 2011, Natur, 480, 344
Oke, J. B., Cohen, J. G., Carr, M., et al. 1995, PASP, 107, 375
Parrent, J., Friesen, B., & Parthasarathy, M. 2014, Ap&SS, 351, 1
Parrent, J. T., Howell, D. A., Fesen, R. A., et al. 2016, MNRAS, 457, 3702
Pereira, R., Thomas, R. C., Aldering, G., et al. 2013, A&A, 554, A27
Perlmutter, S., Aldering, G., Goldhaber, G., et al. 1999, ApJ, 517, 565
Pfannes, J. M. M., Niemeyer, J. C., & Schmidt, W. 2010a, A&A, 509, A75
Pfannes, J. M. M., Niemeyer, J. C., Schmidt, W., & Klingenberg, C. 2010b,
      A, 509, A74
Phillips, M. M. 1993, ApJL, 413, L105
Phillips, M. M., Simon, J. D., Morrell, N., et al. 2013, ApJ, 779, 38
Piro, A. L. 2012, ApJ, 759, 83
Poznanski, D., Prochaska, J. X., & Bloom, J. S. 2012, MNRAS, 426, 1465
Quimby, R. M., De Cia, A., Gal-Yam, A., et al. 2018, ApJ, 855, 2
Raskin, C., & Kasen, D. 2013, ApJ, 772, 1
Raskin, C., Kasen, D., Moll, R., Schwab, J., & Woosley, S. 2014, ApJ, 788, 75
Rest, A., Scolnic, D., Foley, R. J., et al. 2014, ApJ, 795, 44
Riess, A. G., Filippenko, A. V., Challis, P., et al. 1998, AJ, 116, 1009
Riess, A. G., Macri, L. M., Hoffmann, S. L., et al. 2016, ApJ, 826, 56
Riess, A. G., Press, W. H., & Kirshner, R. P. 1996, ApJ, 473, 88
Roming, P. W. A., Kennedy, T. E., Mason, K. O., et al. 2005, SSRv, 120, 95
Rubin, D., Aldering, G., Barbary, K., et al. 2015, ApJ, 813, 137
Saio, H., & Nomoto, K. 2004, ApJ, 615, 444
Scalzo, R., Aldering, G., Antilogus, P., et al. 2014, MNRAS, 440, 1498
Scalzo, R. A., Aldering, G., Antilogus, P., et al. 2010, ApJ, 713, 1073
Schlafly, E. F., & Finkbeiner, D. P. 2011, ApJ, 737, 103
Science Software Branch at STScI 2012, PyRAF: Python Alternative for IRAF,
   Astrophysics Source Code Library, ascl:1207.011
Scolnic, D. M., Jones, D. O., Rest, A., et al. 2018, ApJ, 859, 101
```

```
Shappee, B. J., Prieto, J. L., Grupe, D., et al. 2014, ApJ, 788, 48
Shappee, B. J., Stanek, K. Z., Kochanek, C. S., & Garnavich, P. M. 2017, ApJ,
  841, 48
Shen, K. J., Bildsten, L., Kasen, D., & Quataert, E. 2012, ApJ, 748, 35
Siebert, M. R., Dimitriadis, G., Polin, A., & Foley, R. J. 2020, ApJL, 900, L27
Silverman, J. M., Foley, R. J., Filippenko, A. V., et al. 2012, MNRAS,
  425, 1789
Silverman, J. M., Ganeshalingam, M., Li, W., et al. 2011, MNRAS, 410, 585
Silverman, J. M., Nugent, P. E., Gal-Yam, A., et al. 2013, ApJS, 207, 3
Smith, N., Foley, R. J., & Filippenko, A. V. 2008, ApJ, 680, 568
Stanek, K. Z. 2020, Transient Name Server Discovery Report 2020-50, 1
Szalai, T., Vinkó, J., Könyves-Tóth, R., et al. 2019, ApJ, 876, 19
Tanaka, M., Kawabata, K. S., Yamanaka, M., et al. 2010, ApJ, 714, 1209
Taubenberger, S. 2017, Handbook of Supernovae (Berlin: Springer)
Taubenberger, S., Benetti, S., Childress, M., et al. 2011, MNRAS, 412, 2735
Taubenberger, S., Floers, A., Vogl, C., et al. 2019, MNRAS, 488, 5473
Taubenberger, S., Kromer, M., Hachinger, S., et al. 2013, MNRAS, 432,
Thomas, R. C., Nugent, P. E., & Meza, J. C. 2011, PASP, 123, 237
Tody, D. 1986, Proc. SPIE, 627, 733
Tody, D. 1993, in ASP Conf. Ser. 52, Astronomical Data Analysis Software
  and Systems II, ed. R. J. Hanisch, R. J. V. Brissenden, & J. Barnes (San
  Francisco, CA: ASP), 173
Tucker, M. A., Payne, A. V., Hinkle, J., et al. 2020, Transient Name Server
  Classification Report, 2020-861, 1
Webbink, R. F. 1984, ApJ, 277, 355
Yamanaka, M., Kawabata, K. S., Kinugasa, K., et al. 2009, ApJL, 707, L118
Yamanaka, M., Maeda, K., Tanaka, M., et al. 2016, PASJ, 68, 68
Yoon, S. C., & Langer, N. 2005, A&A, 435, 967
Yuan, F., Quimby, R. M., Wheeler, J. C., et al. 2010, ApJ, 715, 1338
Zhang, K., Wang, X., Zhang, J., et al. 2016, ApJ, 820, 67
```